Chapter

Corrosion Resistance of Precipitation-Hardened Al Alloys: A Comparison between New Generation Al-Cu-Li and Conventional Alloys

Uyime Donatus, Michael Oluwatosin Bodunrin, Ayotunde Olayinka, Mariana Xavier Milagre, Olamilekan Rasaq Oloyede, Sunday Aribo, João Victor de Sousa Araujo, Caruline de Souza Carvalho Machado and Isolda Costa

Abstract

The corrosion resistance of conventional (AA2024-T3, AA6082-T6 and AA7050-T7451) and the new generation (AA2050-T84, AA2098-T351, AA2198-T8, and AA2198-T851) precipitation-hardened alloys has been studied and compared using electrochemical and non-electrochemical approaches. The AA6082-T6 was the most resistant alloy followed by the new generation Al-Cu-Li alloys, except the AA2050-T84. All the alloys exhibited pseudo-passivity, except for the AA2024-T3 alloy which presented the highest number of pitting sites per cm^2 and also exhibited the most insidious form of corrosion amongst the alloys tested. However, the alloy with the highest corrosion depth was the AA2050-T84 alloy followed by the AA2024-T3 and AA7050-T7451 alloys. Intergranular corrosion was associated with rapid rates of penetration. In addition to the microstructural features of the alloys before corrosion, the modes of localized corrosion in the alloys were also influenced by evolving microstructural features (such as re-deposited Cu) during corrosion.

Keywords: wrought Al alloys, new-generation Al alloys, localized corrosion, microstructure, SEM

1. Introduction

New generation Al alloys are being developed to meet lightweight requirements in the automotive and aerospace sectors. For a successful introduction, the alloys must possess specific strengths, mechanical properties and corrosion resistance superior or at least equal to those exhibited by conventionally used Al alloys. Concerning corrosion, the currently used high strength 2xxx and 7xxx series alloys

in the aerospace sector are highly susceptible to severe localized corrosion (SLC), but adequate care should be taken in ensuring that the proposed replacements (the new generation Al-Cu-Li alloys) exhibit better in-service corrosion performances.

There are reports in the literature [1–3] comparing the corrosion resistance of selected conventional alloys to that of the new generation Al-Cu-Li alloys, and most of these studies were based on the use of electrochemical techniques [1, 3]. However, electrochemical techniques alone cannot give enough information about the corrosion behavior of these alloys. This is because electrochemical techniques are largely designed to generate data from activities occurring on the surfaces of materials. Sub-surface details from tens to hundreds of microns beneath the surface are very difficult to obtain via electrochemical methods. Attacks in precipitation-hardened aluminum alloys can penetrate hundreds of microns beneath the surface as fissures with non-linear pathways that are difficult to follow from the surface. This is in addition to the fact that the attacks can also transit easily from one form to the other, and the active area of corrosion is very difficult to establish [4].

Thus, it is always important to examine the surfaces and cross-sections of the corroded alloys via microscopic techniques before concluding. In this regard, it is also important to mention that conclusions from nano to mesoscale microscopic approaches should be drawn with caution because even macro/microscale results can be very misleading if care is not taken.

In this work, the comparison between the corrosion resistance of the new generation Al-Cu-Li alloys and that of conventional aluminum alloys have been made using scanning electron microscopy with the results correlated with potentiodynamic polarization results. Alloys from all the precipitation-hardened series (2xxx, 6xxx and 7xxx) were selected. The selected alloys are industrial alloys in the common tempers in which they are being employed. These alloys derive their strengths from the formation of finely and uniformly distributed nano-sized phases in their matrix. To accomplish the precipitation of these phases, alloying elements with reducing solid solubility as temperature decreases are used for this purpose. Examples of elements that fall into this category include, copper, magnesium, zinc and, lithium. The potentials of the intermetallic particles formed by these elements are often different from that of the matrix (i.e. these particles are either cathodic or anodic to the matrix) when exposed to aggressive environments, and this results in the development of localized corrosion which compromises the integrity of the alloys in service. The form and extent of localized corrosion are alloy specific. Establishing the severity and how insidious the different forms of attacks in competing alloys are crucial to improving the performance of the components built from these alloys. Thus, in this work we have compared the forms and how insidious the corrosion attacks in selected industrially important alloys are, especially by contrasting between the attacks in new generation and conventional aluminum alloys in sea-water environment.

2. Experimental

The conventional alloys employed in this study are the AA2024-T3, AA6082-T6 and the AA7050-T7451 alloys, and the new generation alloys are the AA2050-T84, AA2098-T351, AA2198-T8 and AA2198-T851 alloys. The compositions of these alloys are as presented in **Table 1**. These alloys are commercial alloys in the tempers in which they are mostly employed.

Prior to the corrosion tests, the samples were sequentially polished to a 1 μm surface finish using SiC papers and diamond pastes.

	Cu	Li	Fe	Zr	Cr	Mg	Zn	Si	Mn	Ag
AA2024-T3	4.2		0.2		0.1	1.6	0.2	0.1	0.4	0.15
AA2050-T84	3.64	1.0	0.04	0.12		0.36	0.02		0.39	
AA2098-T351	3.4	1.0	0.04	0.4		0.3	0.02	0.05	0.003	0.3
AA2198-T8	3.32	0.96	0.005	0.51		0.31	0.004	0.004	0.002	0.26
AA2198-T851	3.31	0.96	0.004	0.4		0.31	0.01	0.03		0.25
AA6082-T6			0.33			0.74	0.05	0.71	0.40	
AA7050-T7451	2.15		0.04	0.14		1.53	6.80	0.08		

Table 1.
Composition (wt. %) of the alloys used in this study.

The main investigation in this work was based on optical and scanning electron microscopy of the surfaces and cross-sections of the alloys after a 72 h corrosion immersion test in 3.5% NaCl solution. Polished samples of the alloys were employed, and beeswax was used to expose an area of 1 cm^2 on the alloys.

Other corrosion tests employed in the investigation were potentiodynamic polarization tests, agar-gel visualization test and scanning vibrating electrode technique (SVET) measurements.

Potentiodynamic polarization curves of the alloys were obtained in the 3.5% NaCl solution. A three-electrode cell comprising the sample as the working electrode, an Ag/AgCl reference electrode and a platinum wire as a counter electrode was employed for the polarization tests. The scans were initiated at −100 mV of the open circuit potential (OCP) values to +800 mV of the OCP. OCP measurements were conducted for 90 min prior to the polarization measurements, and a scan rate of 1 m V/s was employed.

Details of the agar-gel visualization test are similar to those reported in previous work from the same group [5], except that a universal indicator was employed this time in the place of phenolphthalein.

For the scanning vibrating electrode technique (SVET) measurements, an Applicable Electronic Produced SVET machine with an ASET 4.0 software was employed using a 5 mM NaCl solution. SVET maps and optimal images were obtained every 2 h. Further details on the SVET procedures can be found in a previously published work from the same group [6].

Scanning electron microscopy (SEM) analysis was conducted using a JEOL JEM 6010 LA and TM 3000 microscopes equipped with an energy-dispersive x-ray spectroscopy (EDS) detector. Transmission electron microscopy (TEM) was conducted using a JEM-2100F microscope. The TEM samples were prepared by twin-jet electropolishing using 35% nitric acid in methanol after an initial thinning through grinding with SiC papers.

3. Results and discussion

The results of the corrosion studies are presented in two parts. Firstly, results from electrochemical analyses are presented and compared. Majorly, potentiodynamic polarization and SVET results are compared, while agar visualization test was employed to understand the pH variation around an SLC site further. Subsequently, SEM examination of the surfaces and cross-sections of the alloys are presented and compared.

3.1 Electrochemical tests

3.1.1 Potentiodynamic polarization

Presented in **Figure 1** are the potentiodynamic polarization results of the selected alloys in 3.5% NaCl solution. **Figure 1a** combines the potentiodynamic polarization curves of all the alloys investigated, while **Figure 1a, b** shows the curves of the new generation Al-Cu-Li alloys (AA2050-T84, AA2098-T351, AA2198-T8 and AA2198-T851) and the curves of the conventional alloys (AA2024-T3, AA6082-T6 and AA7050-T7451), respectively. **Figure 1d** is a plot of extrapolated corrosion potential (Ecorr) and pitting potential (Epit) values for the different alloys from the plots in **Figure 1a** (The Epit, in this case, is the potential beyond which there is a large increase in current density compared with the pseudopassive region just above the Ecorr). These results show that, amongst the new generation alloys, the AA2050-T84 alloy with the lowest Ecorr value (≈−0.82 V) exhibited the highest tendency to corrode, while the AA2098-T351 and AA2198-T8

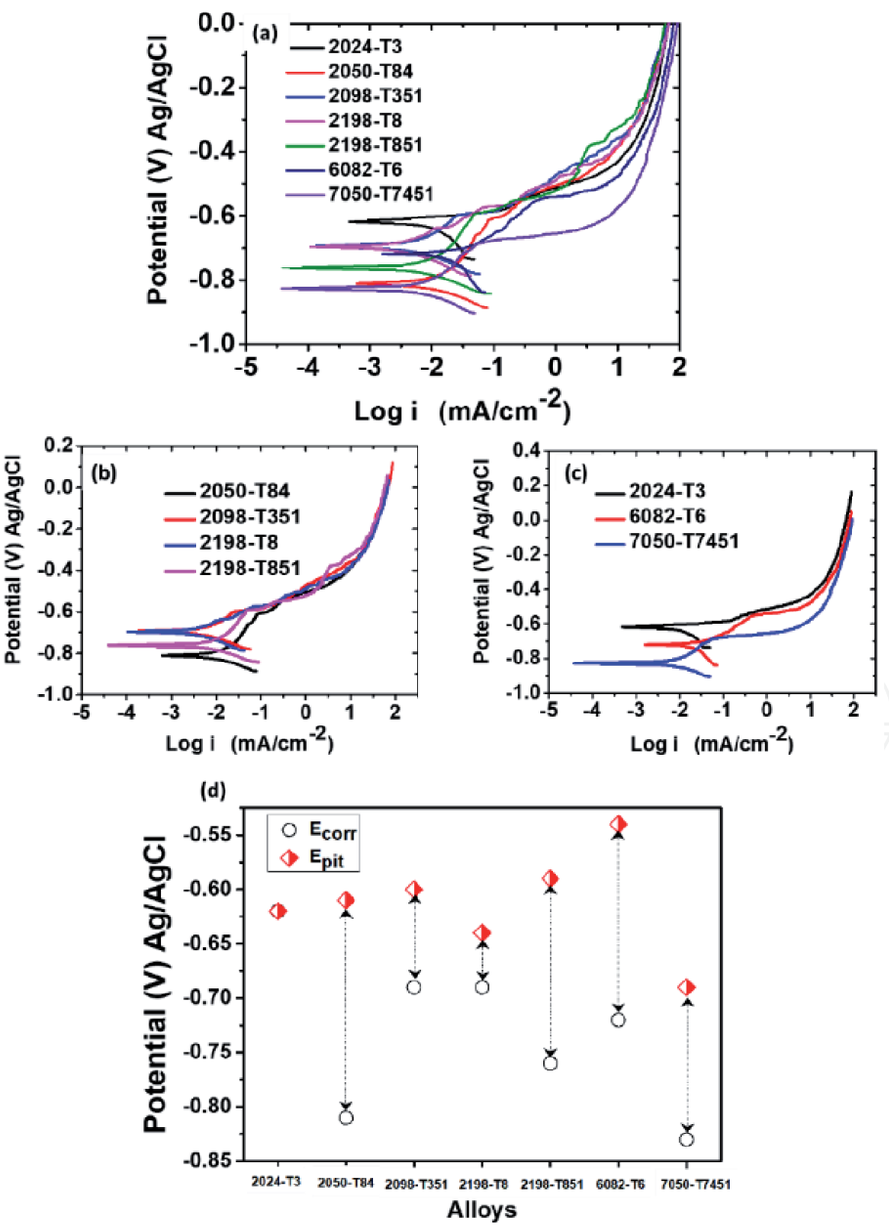

Figure 1.
Potentiodynamic polarization results of selected heat-treatable aluminum alloys in 3.5% NaCl solution.

alloys, with the highest Ecorr values (≈−0.68 V), exhibited the lowest tendency to corrode. The Ecorr value (≈−0.76 V) of the AA2198-T851 alloy was in between those of the AA2050-T84 and AA2098-T351/2198-T8 alloys indicating that the AA2198-T851 alloy has more corrosion tendency than the AA2098-T351/2198-T8 alloys but lower tendency than the AA2050-T84 alloy.

Nonetheless, all the new generation alloys exhibited pseudo-passive behavior under the conditions tested. The Epit – Ecorr difference shows the potential range for the active – pseudopassive behavior. Pseudopassivation occurs because of the formation of a non-protective oxide layer on the alloys [7, 8]. It should be noted that the Epits in these alloys are not the actual pitting potentials of the alloys. These alloys develop severe localized corrosion at OCP (i.e. at potentials lower than the pseudopassive range). The oxide formed after the active regions is only formed on non-pitting sites. And the contribution of the pitting sites to the total current is overshadowed by the current flowing from the larger surface with an oxide layer [8]. Thus, the pseudopassive current predominates at this potential range. However, after the potentials designated as Epits, the contribution of the pitting areas to the overall current flowing from the surface becomes significant [8] and superior to the pseudopassive current, and this leads to pronounced current density increase per potential.

For the conventional alloys, the AA7050-T8451 alloy, with an Ecorr value in the range of ≈−0.84 V, exhibited the highest tendency to corrode, followed by the AA6082-T6 alloy with an Ecorr value of ≈−0.72 V. The AA2024-T3 alloy, with an Ecorr value of ≈−0.63 V, exhibited the lowest tendency to corrode. Amongst the three conventional alloys compared, the AA2024-T3 alloy did not show any pseudo-passive range in the condition tested. In fact, amongst all the alloys compared, the AA2024-T3 alloy was the only alloy that did not exhibit a pseudopassive behavior. This implies that the contribution of the pitting areas to the total current was significant (from potentials equal to or below the Ecorr) and swamped that from the oxide-covered surface. Thus, the AA2024-T3 alloy possibly presented a higher active pitting area compared with the other alloys.

Nonetheless, for all the alloys, AA2024-T3 > AA2098-T351/AA2198-T8 > AA608 2-T6 > AA2198-T851 > AA2050-T84 > AA7050-T7451 in terms of Ecorr values. Based on this, the AA7050-T7451 alloy exhibits the highest tendency to corrode and should be the most susceptible to corrosion amongst all the alloys. The AA7050-T7451 alloy also presented the lowest potential at which the current from the pitting areas contributes significantly to the total current flowing from its surface. Also, it is expected that the AA2024-T3 alloy should exhibit the least tendency to corrode in NaCl environment amongst the alloys investigated. Also, since the new generation alloys have lower Ecorr values compared with the AA2024-T3 alloy, the new generation Al-Cu-Li alloys should be more susceptible to corrosion compared with the AA2024-T3 alloy.

However, potentiodynamic polarization results are not sufficient to establish the corrosion resistance of these alloys, especially as it is difficult to rely on extrapolated current density values for aluminum alloys in near-neutral NaCl environments. One of the reasons being that it is difficult to establish the active corroding area [4]. For a quick comparison, SVET immersion tests were conducted on samples representing the Al-Cu-Mg, Al-Cu-Li, Al-Mg-Si and Al-Zn-Mg series as presented in the section below.

3.1.2 SVET immersion tests

Figures 2 and **3** present the SVET result of the AA2024-T3 (Al-Cu-Mg), AA2198-T851 (Al-Cu-Li), AA6082-T6 (Al-Mg-Si) and AA7050-T7451 (Al-Zn-Mg)

alloys after 2 and 18 h of immersion (Two 2xxx series alloys were selected to have a conventional (AA2024-T3) and a new generation Al-Cu-Li alloy (AA2198-T851) representation. Also, the solution employed in this case was 5 mM NaCl solution. This solution is less aggressive compared with the 3.5% NaCl solution since it contains less chloride ions, and it was chosen to allow for easy monitoring of the in-situ corrosion activities on the alloys with time.)

Pronounced anodic activities were observed on the AA7050-T7451 and AA2024-T3 alloys within the first 2 h of immersion (**Figure 2**). The SLC sites were easily discernible on the AA2024-T3 alloy (**Figure 2b**) but difficult to find on the AA7050-T7451 alloy (**Figure 2h**) at macroscale because of the nature of pit covering and corrosion product formation on the later alloy (this is discussed further in the section below). For the AA2198-T851 alloy, the anodic activities were not that pronounced (compared with these two alloys), and only traces of SLC sites were observed (an example is indicated by the red arrow). Localized activities associated with SLC were not observed on the AA6082-T6 alloy. The localized activities observed in the early hours were transient and no stable SLC site was initiated on this alloy after 2 h.

In the later hours of the test, the anodic activities were reduced at the surfaces of the AA2024-T3 and AA7050-T7451 alloys were pronounced SLC activities were observed because corrosion products had covered the sites on the AA7050-T7451 and AA2024-T3 alloys. At this stage, visible SLC sites were evident on the AA2198-T851 alloy. However, corrosion products also formed on these sites and reduced the anodic activities recorded by the SVET. Again, for the AA6082-T6 alloy,

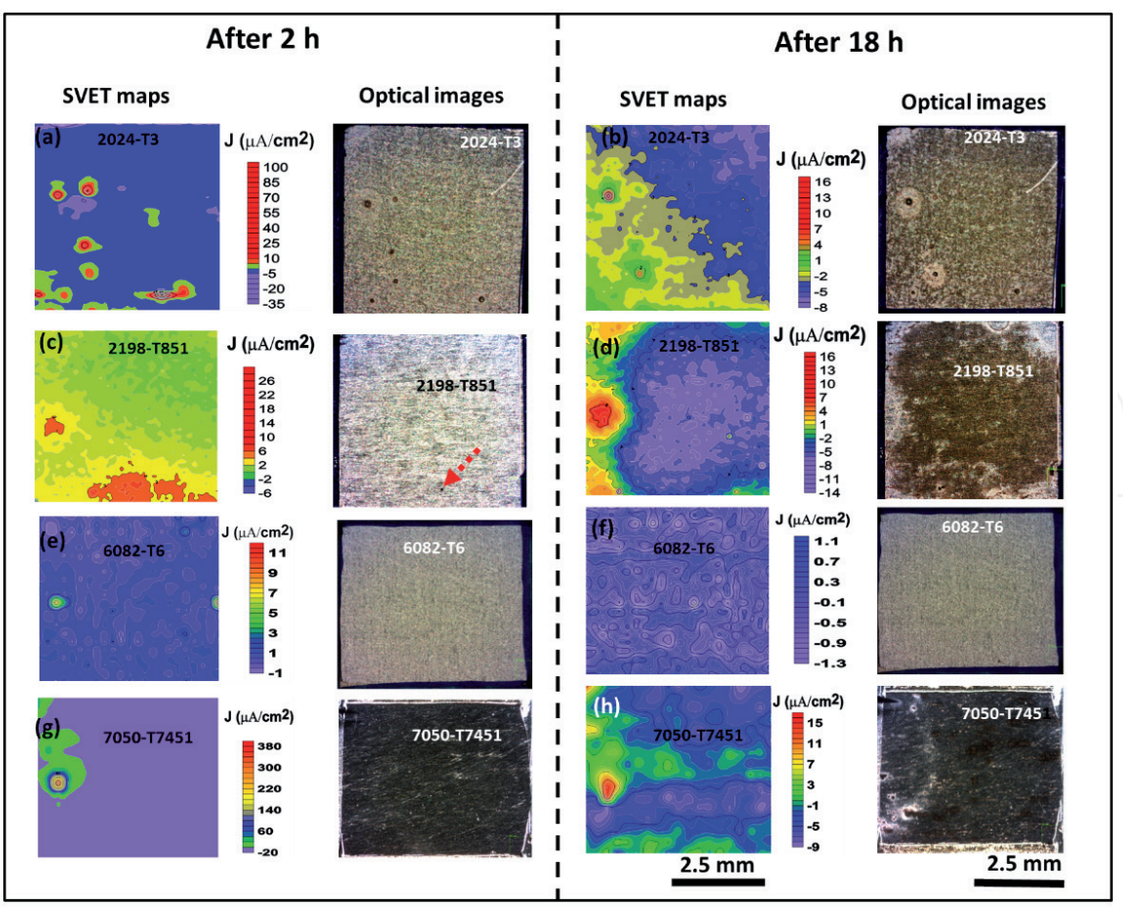

Figure 2.
SVET current density maps and optical images of the tested alloys in 5 mM NaCl solution after 2 and18 h of immersion.

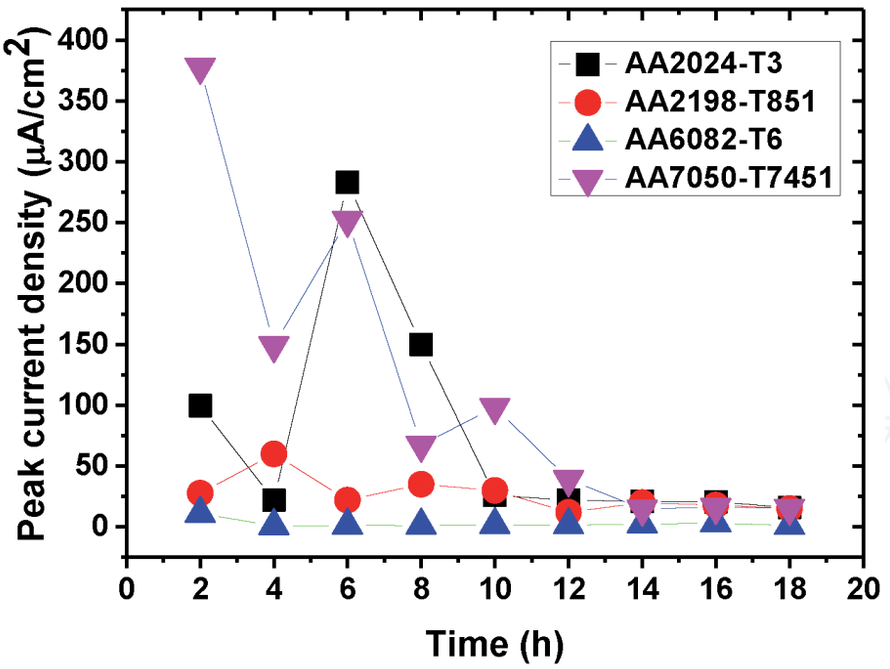

Figure 3.
Plots of peak current density values recorded on the alloys during the SVET immersion test.

no trace of SLC activity was recorded by the SVET and the optical macrograph also did not reveal any trace of SLC site.

Presented in **Figure 3** is a plot of the peak current density recorded on the alloys throughout the test. As evident, the highest peak current density values were recorded on the AA2024-T3 and AA7050-T7451 alloys. Peak current density values as high as 298.3 and 377.8 μA/cm^2 were recorded on both alloys, respectively. Lower peak current density values were recorded on the AA2198-T851 alloy with the highest being in the range of 60 μA/cm^2. For the AA6082-T6 alloy, the peak current density values were near zero with the highest being about 11 μA/cm^2. The average peak current density values recorded on these alloys were 114.49 μA/cm^2 for AA7050-T7451, 73.03 μA/cm^2 for AA2024-T3, 21.0 μA/cm^2 for AA2198-T851 and 2.38 μA/cm^2 for AA6082-T6. This implies that the AA7050-T7451 alloy was the most susceptible and the corrosion rate on the alloy was the highest. However, it should be noted that the peak current values on this alloy were emanating from a few SLC sites compared with the AA2024-T3 alloy. The number of SLC sites were highest on the AA2024-T3 alloy, and high current density values were emanating from multiple sites across the surface of the alloy. This possibly explains why no pseudo-passivity was observed on the AA2024-T3 alloy during potentiodynamic polarization, since the sum of the current from the pitting sites would be very significant, swamping the total current flowing from the oxide-covered area.

The SEM images of the surfaces of the alloys before the removal of corrosion products show SLC sites on the AA2024-T3, AA7050-T7551 and AA2198-T851 alloys but not on the AA6082-T6 alloy (not even trenching associated with the cathodic Al-Fe-Si rich phases were observed on the AA6082-T6 alloy). The reason for the immaculate corrosion resistance of the AA6082-T6 alloy in the test environment used may be because of the insignificant amount of Cu. Galvanic coupling activities associated with Cu-rich particles are often more pronounced than those associated with Fe and Si-rich particles. The AA6082 alloy is, however, susceptible in chloride environment when Mg_2Si particles are precipitated in the presence of precipitate free zones (PFZs) at the grain boundaries (GBs), and this is most common in the weld heat-affected zones and overaged temper (T7) of the alloy. For the other alloys,

the microstructural factors associated with the formation of SLC are readily present in their microstructure in the present tempers. These factors include S-phase and Cu-rich particle clusters for the AA2024, η phase (and its variants) and PFZs for AA7050, and T1 particles for the AA2198 alloy.

The SLC sites on these susceptible alloys were covered with corrosion products, and these sites were found within corrosion rings (especially as showcased in the SEM image of the AA2198-T851). The observed corrosion rings resulted from pH difference between the regions around the SLC pits and the surroundings. The reduction reaction of dissolved oxygen occurs in the surrounding region, while H^+ ions are generated from the hydrolysis of Al^{3+} inside the pit. During the pitting process, the H^+ ions migrate from within the pits to the mouths of the pits due to electrostatic potential difference [9]. Thus, H^+ ions are present around the pit/SLC site and cause a local reduction in the pH around the pit mouths as evident in the agar-visualization result in **Figure 4a–d** (see the evolution of the sites labelled 1 and 2). Also, although the predominant reduction of H^+ to generate H^2 bubbles occurs inside the pits, some of the ions are reduced around the pit mouths. What is clear, as will be seen in the section below, is that there is a boundary between the low pH region around the SLC sites and the high pH region surrounding the sites, and this boundary defines the domain of the corrosion rings as clearly depicted by the black arrow of the site labelled 2 in **Figure 4a–d**. The site labelled 1.

SEM analysis was further carried out after the removal of corrosion products on the surfaces of the alloys that exhibited SLC. In agreement with the SVET peak current density values, the width and extent of the attack on an SLC site were most pronounced on the AA7050-T7451 alloy. However, those of the AA2024-T3 were not as pronounced as expected especially when compared with those on the AA2198-T851 alloy. Intergranular corrosion (IGC) expanding only within about 70 μm was observed on the surface of the AA2024-T3 alloy, whereas intragranular corrosion expanding beyond 100 μm was observed on the AA2198-T851 alloy. Also, it appears as if more

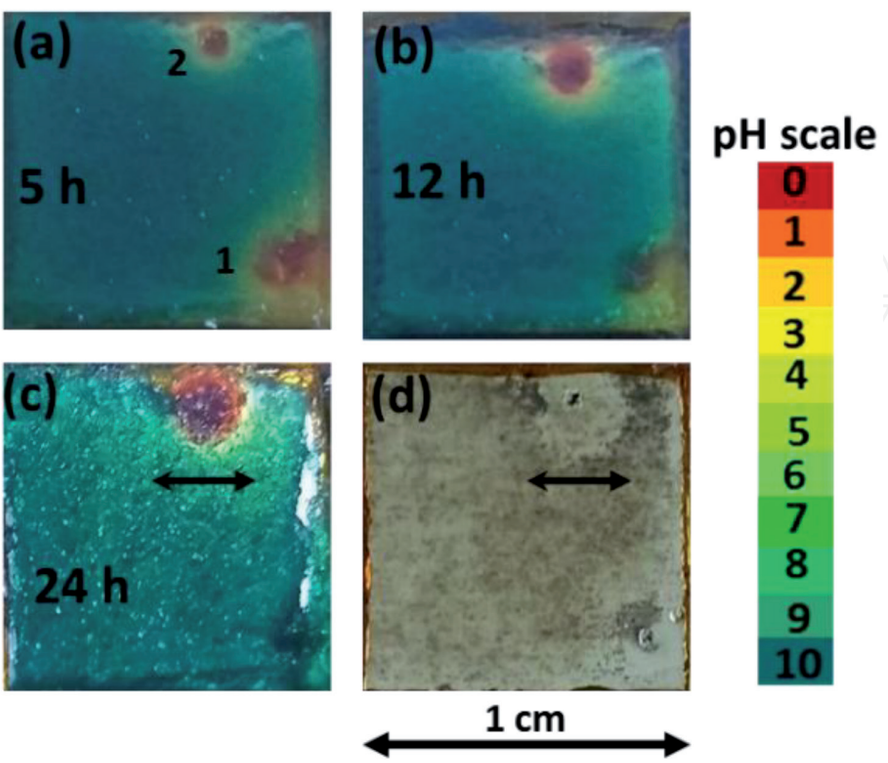

Figure 4.
Optical images showing the pH around SLC sites on AA2198-T851 alloy during agar visualization test and the corresponding surface after the removal of the gel.

materials were consumed on the AA2198-T851 alloy compared with the AA2024-T3 alloy. From these two alloys, the widths and the intensity of corrosion observed from the SEM images do not appear to correlate well with the current density values recorded during the SVET measurements. The peak current density values and the number of SLC sites indicate that the AA2024-T3 alloy was more prone to corrosion compared with the AA2198-T851 alloy. However, the SEM images of the surfaces after the corrosion test, tend to indicate otherwise. Also, the diameters of the corrosion rings were larger on the AA2198-T851 alloy compared with the AA2024-T3 alloy.

Nonetheless, the SVET results indicate that in order of rate of corrosion attack the AA7050 > AA2024 > AA2198-T851 > AA6082-T6 alloy. Thus, except for the AA6082-T6 alloy which exhibited no trace of corrosion during the test, the new generation AA2198-T851 Al-Cu-Li alloy is better than the conventional AA2024-T3 and AA7050-T7451 alloys. However, it is difficult to relate the observed SVET results to those of the potentiodynamic polarization curves of the alloys based on Ecorr values. The only relatable correlation is the magnitude of the current density values, which is quite high for the AA2024 alloy in agreement with the predominance of the pitting current over the pseudopassive current from OCP as observed on the potentiodynamic polarization curve. Thus, to get more details in a bid to establish the corrosion resistance of the alloys, a non-electrochemical approach is needed.

3.2 Non-electrochemical approach

The non-electrochemical approach employed in this study involves optical and scanning electron microscopy analyses of the surfaces of the selected alloys after a 72-h immersion test. The surfaces were examined before and after the removal of corrosion products. Following these, cross-sectional examinations of the corrosion attacks were then carried out.

Presented in **Figure 6** are the optical images of the surfaces of the alloys after the immersion test. The new generation Al-Cu-Li alloys are placed on top—**Figure 7a–d**, while the conventional alloys are placed below, **Figure 6e–g**. At this scale, discernible SLC pits were pronounced on the new generation Al-Cu-Li alloys with the AA2050-T84 alloy appearing to exhibit the most number of pitting sites. The conventional alloys did not exhibit pronounced discernible pitting sites except for the AA7050-T7451 alloy (as depicted by the arrow). However, similar to the SVET sample, the surface of the AA7050-T7451 alloy was glossy and did not show any trace of corrosion (except for the area depicted with red arrow). No trace of SLC was found on the AA6082-T6 alloy at this scale. The AA2024-T3 alloy also appeared to show no trace of SLC sites when wet. However, after the surface was dried under an air stream, multiple SLC sites appeared to be present on the surface of the alloy. Thus, the optical micrographs presented tend to show that the new generation Al-Cu-Li alloys are more prone to corrosion compared with the conventional alloys. Amongst the conventional alloys, the AA6082-T6 appeared to be the most resistant compared with the other two alloys.

However, polarization curves show that the AA6082-T6 and AA7050-T7451 alloy have high tendencies to corrode in the test environment. Thus, it is necessary to examine the extent of corrosion further at higher magnifications. In this regard, the surfaces of the corroded alloys and the cross-sections are examined using the SEM.

3.2.1 New generation Al-Cu-Li alloys

3.2.1.1 AA2050

Figure 5 presents the SEM images of the corroded surface and cross-section of the AA2050 alloy before and after the removal of corrosion products. The SLC sites

were situated within corrosion rings. The number of SLC sites per cm^2 was about 14. The corrosion features observed on the surface of the alloy suggest that the attack was predominantly intergranular, and the attacks were aligned according to

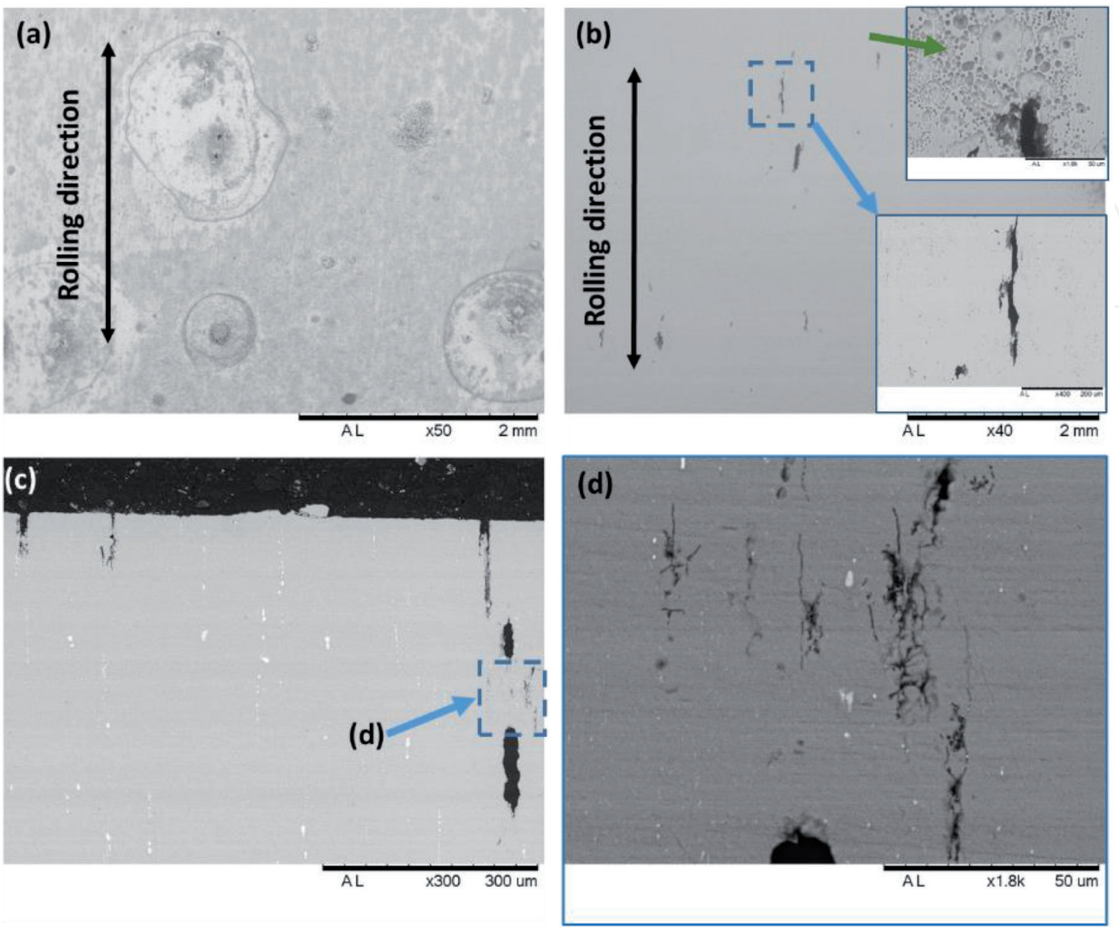

Figure 5.
SEM images of the corroded (a, b) surface of AA2050-T84 alloy ((a) before and (b) after the removal of corrosion products) and (c, d) cross-section showing the depth and different SLC types in the alloy.

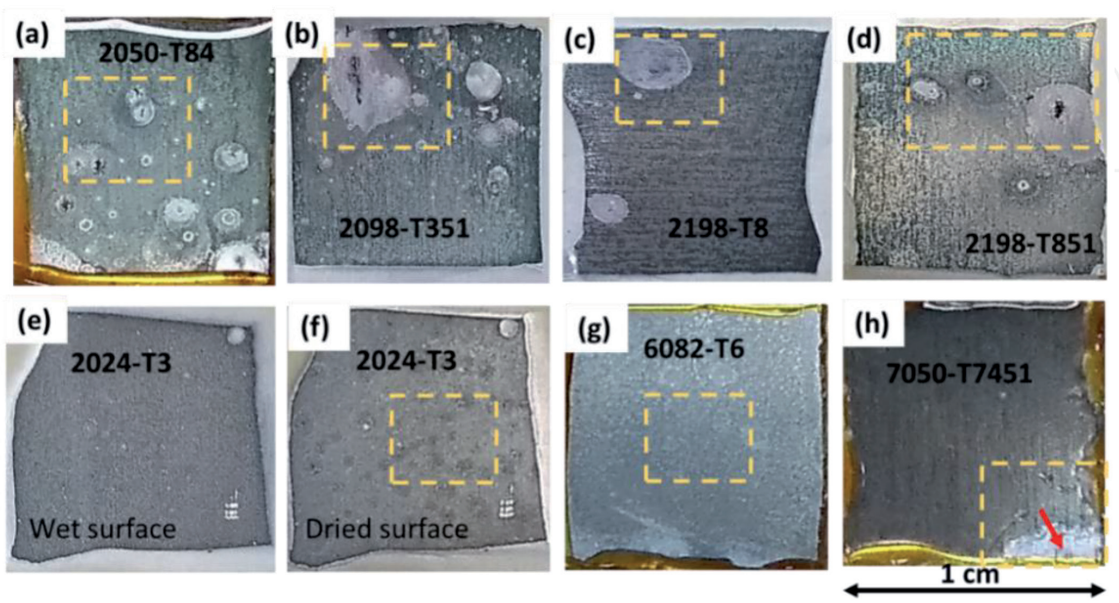

Figure 6.
Optical images showing the corroded surfaces of selected aluminum alloys after 72 h immersion in 3.5% NaCl solution at macroscopic scale.

the direction of deformation (see the inset from the region highlighted with blue rectangle in **Figure 5b**). In certain regions, superficial attacks were observed at the mouths of the pits (as indicated by the green arrow in the inset **Figure 5b**). It does appear as if the corrosion products from the pit preferentially etches the surface around the pit mouth. As earlier mentioned, H^+ ions migrate from within the pits to the mouths of the pits. This migration results in the decrease of the pH near the pit mouths. Thus, the local chemistry around the pit mouth is different from those in the surroundings. In this region, the solution can be aggressive owing to the reduced pH which can result in the mild attack of the surface of the alloy.

Cross-sectional images of the corroded AA2050-T84 alloy are presented in **Figure 5c, d** and **Figure 8a, b**. Attacks were observed penetrating as deep as 420 μm beneath the surface. Also, both intergranular and intragranular attacks were observed. The observed attack morphologies suggest that the attack initiated as IGC and then transited to intragranular. The magnified images in **Figure 8** show the typical progression of the attack. Cu-rich particles were observed to promote the dissolution of the adjacent matrix in the direction of corrosion propagation. Non-uniform precipitation was also observed as depicted in the images. The A-regions were richer in particles than the B-regions. This may affect the rapid propagation of the attack as observed since a galvanic cell will be most likely created between the particle-rich bands and the bands with lesser particles. Another interesting feature was the activities of redeposited Cu (**Figure 8b**). The re-deposited Cu promoted the dissolution of the matrix in a version similar to the Cu-rich particles. This sort of secondary attack caused the transition of the attack from intergranular to intragranular.

In the AA2050 alloy, initiation of IGC has been associated with Cu and Li enrichment of the GBs although reports are associating the corrosion susceptibility of the AA2050 alloy with the activities of T1 particles at the GBs [10, 11]. A recent detailed report by Yan et al. [12] has shown that IGC attacks are most likely due to Cu-Li enrichment or the presence of S-phase at the GBs. Also, Guerin et al. [13] showed that, even though the T1 precipitates populated the GBs in AA2050 alloy, the IGC observed in the T34 alloy was not due to the activities of the T1 phase. Other factors, such as high level of misorientation, were suggested to have more influence on IGC susceptibility. Thus, the attack observed in this work probably initiated at the GBs due to Cu and Li enrichment of the GBs, but the transition to intragranular corrosion occurred due to non-uniform precipitation, the presence of cathodic Cu-rich coarse particles in the corrosion paths, and the activities of re-deposited Cu which acted as local cathodic sites for the dissolution of the adjacent matrix.

3.2.1.2 AA2098-T351, AA2198-T8 and AA2198-T851

The corrosion behaviors of these alloys are very similar, and this is why they are grouped in this section. **Figure 7** presents the SEM images of the surfaces and cross-sections of the AA2098-T351 alloy. The corrosion features in the three alloys are similar.

These alloys exhibited SLC sites formed within corrosion rings, and the attacks spread on the surfaces of the alloy with re-deposited Cu at the edges of the attacks. From the examination of the images of the surfaces after the removal of the corrosion products, it was observed that the attacks spread laterally with that of the AA2098-T351 alloy being the most pronounced (as much as 2 mm). In addition to the lateral spread, undercutting also occurred for the three alloys. Furthermore, the number of pits per area were significantly lower compared with the AA2050-T84 alloy - ranging between 3 and 8 per cm^2 for the three alloys. The AA2198-T8 alloy was the least susceptible to corrosion. It exhibited the lowest number of pits per

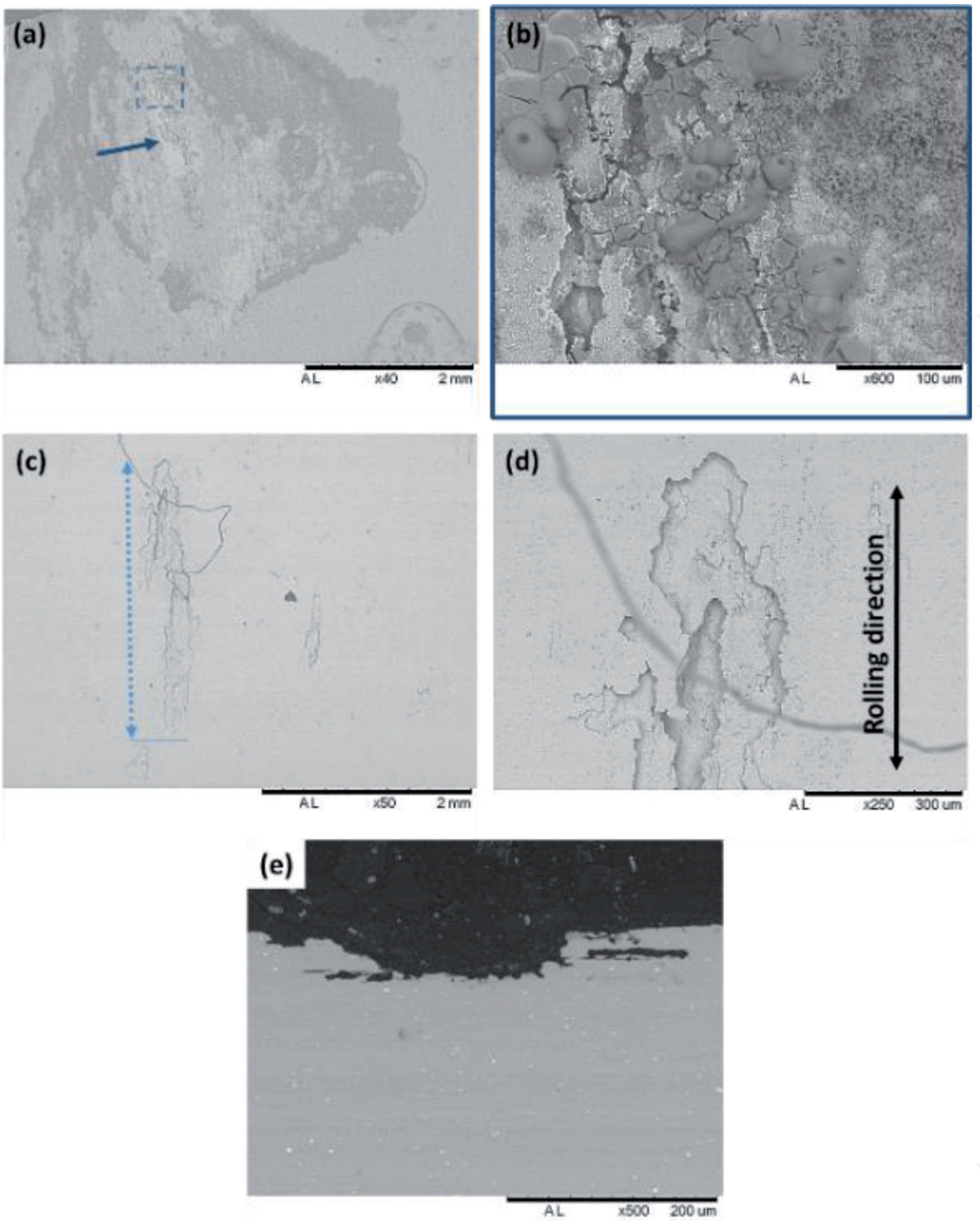

Figure 7.
SEM images of the corroded surface of AA2098-T351 alloy (a, b) before and (c, d) after the removal of corrosion products. (e) A cross-sectional view of the corrosion.

area and the depth of attack was only in the range of 50 μm. The depth on the AA2098-T351 alloy was around 70 μm. The most susceptible of the three alloys was the AA2198-T851 alloy. The attack depth on this alloy was as much as 110 μm. The reason for the increased susceptibilities of the AA2098-T351 and AA2198-T851 alloys to corrosion is because of the "51" temper treatment. This treatment involves an extra deformation process which introduces more dislocations into the alloys. Dislocations are preferred sites for the precipitation of the T1 phase which is the phase responsible for the formation of SLC in these alloys [6, 14–19]. Thus, the AA2198-T851 and AA2098-T351 alloys contain more T1 particles, particularly the AA2198-T851 alloy since it is artificially aged. The higher densities of the TI particles in these two alloys make them more susceptible compared with the AA2198-T8 alloy. And this is

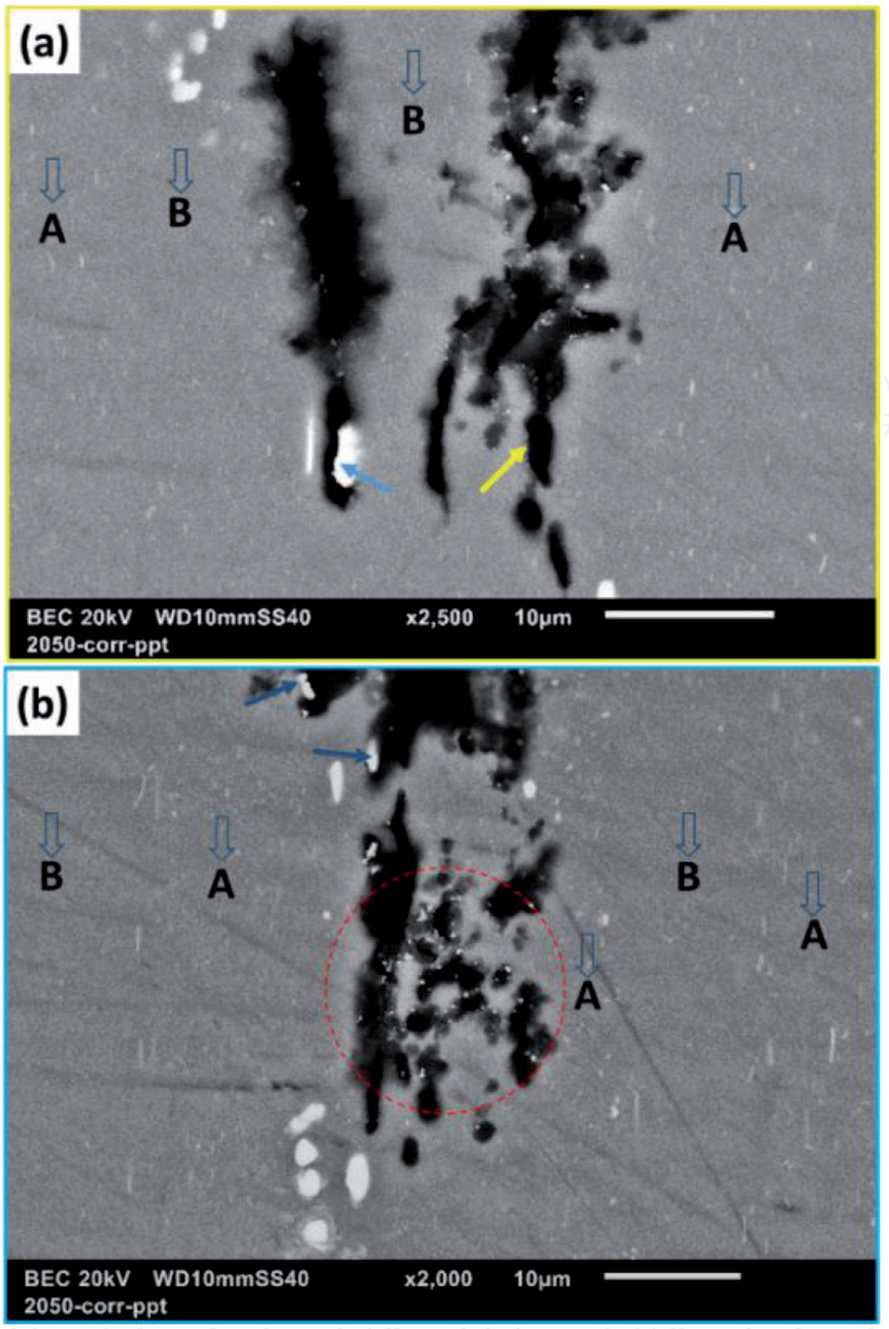

Figure 8.
SEM images of the cross-section of AA2050-T84 alloy showing SLC morphology and non-uniform precipitation in the alloy.

evident in the depths and spread of the attack. Nonetheless, the attacks on the three alloys spread more laterally and did not penetrate to very high depths as observed on the AA2050-T84 alloy. These three alloys, the AA2098-T351, AA2198-T8 and AA2198-T851, did not exhibit any form of intergranular corrosion. Also, it is important to note that the coarse intermetallic particles in these alloys are not associated with the initiation of SLC. The coarse particles cause the localized dissolution of the surrounding matrix, and, consequently are associated with the formation of trenches and cavities (micro-pits).

The increased depth in the AA2050-T84 alloy may be associated with the highly localized regions of attack with pronounced non-uniform precipitation in bands. Another important factor to note is that the SLC initiation in the AA2098-T351, AA2198-T8 and AA2198-T851 alloys is associated with the T1 phase which is present in the interiors of the grains as shown in **Figure 9**. This results in the intragranular

attack observed. The GBs in these alloys are resistant to corrosion as shown in previous works from the same group [20, 21]. On the other hand, the SLC initiation in the AA2050 alloy is associated with Cu and Li enrichment at the GBs [12]. This results in intergranular corrosion which transits to intragranular (due to the effects of non-uniform precipitation, cathodic Cu-rich particles and Cu-redeposition) and penetrates very deep into the alloy. Thus, the corrosion behaviors of the new generation Al-Cu-Li alloys are not the same, the corrosion morphology and rate in the AA2050 alloys are very different from those of the other new-generation Al-Cu-Li alloys. For the later alloys, the attacks propagate laterally, predominantly. What is however common amongst the alloys is that irrespective of whether the attacks are penetrating deeply into the alloy or spreading laterally, the deformation the alloys were previously subjected to played a role in the propagation of attacks. In the AA2098 and AA2198 alloys, the attacks spread laterally according to the rolling direction. Also, in the AA2050 alloy, the attack spread and penetrated according to the rolling effect. Thus, in these alloys, there is a relationship between deformation and the propagation of SLC.

3.2.2 AA2024-T3 alloy

Figure 10 presents the SEM images of the surface of the AA2024-T3 alloy before and after the removal of corrosion products. Before the removal of corrosion products, it was difficult to locate the SLC sites. After the removal, small-sized SLC sites were observed all over the surface of the alloy. The number of SLC sites per area was more than 400. The cross-sectional images presented in **Figure 11** shows the attack depths and the corrosion morphologies. The region in brown square region in **Figure 11a** is further analyzed in **Figure 12**. **Figure 11c** and **11d** are magnified images of the blue and green square regions in **Figure 11a** and **11b**, respectively. The red arrows indicate intergranular attack, the blue arrows indicate trenched particles and the yellow arrows indicate regions that have been attacked intergranularly. Attacks were observed to have penetrated as deep as 220 μm. Thus, the attack on

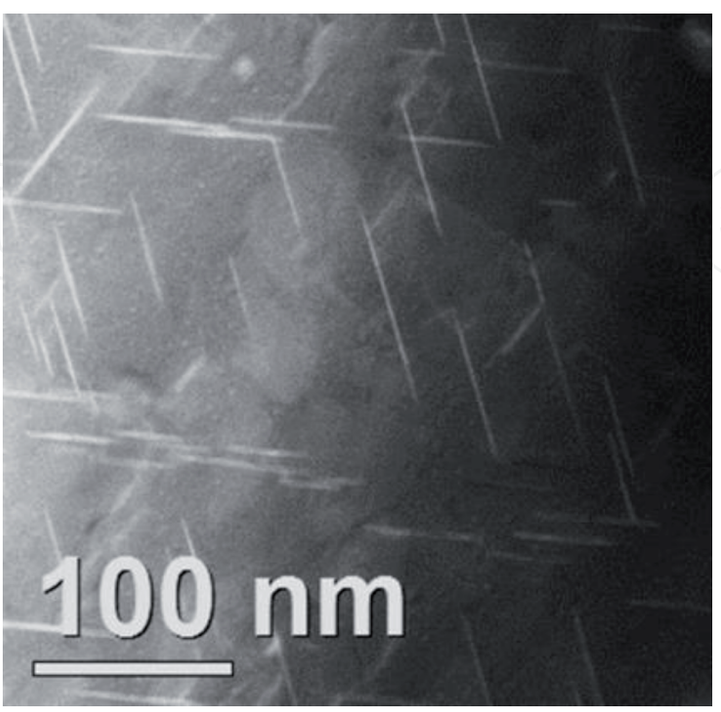

Figure 9.
HAADF image of the grain interior of AA2198-T851 alloy showing the typical hexagonal T1 precipitates present in new generation Al-Cu-Li alloys.

this alloy is very insidious since numerous small-sized attacks are penetrating very deep into the alloy without pronounced signs at the surface, especially during corrosion as shown by the differences between the wet and dried surface in **Figure 6**.

SLC attacks in AA2024 alloy are usually nucleated at regions with clusters of Cu-rich particles irrespective of whether they are S-phase particles or not [22–27]. However, in this work, most of the particles analyzed in the vicinity of attacks were predominantly S-phase particles. This is not surprising since the S-phase constitutes more than 60% of the coarse intermetallic particles present in the AA2024 alloy [28]. The S-phase associated attack resulted in pitting and transition to intergranular attack as the attack propagated. This is reflected in **Figure 11**, where trenching around cathodic particles are also revealed. Also, partial consumption of particles which resulted from the heterogeneities of the individual particles was observed (**Figure 12**).

With respect to the attack features, three types of coarse particles were observed (**Figure 12**): highly heterogeneous particles (HT); more homogeneous particles (HM); and high Cu-containing particles (HC). Partial dissolution of particles is associated with the HT particles. From **Figure 12**, it can be seen that the HT particles contain regions that are richer in Cu relative to the other regions of the particles. The EDX analysis of the observed HT particles revealed that they were predominantly Al-Cu-Mg particles with significant differences in the weight percentages of the three elements. For instance, in one of the particles, the Al, Cu, Mg weight percentages were 25.16, 63.69 and 1.23, respectively, in one region and 35.29, 49.02 and 12.59 in another region. The presence of multi-components

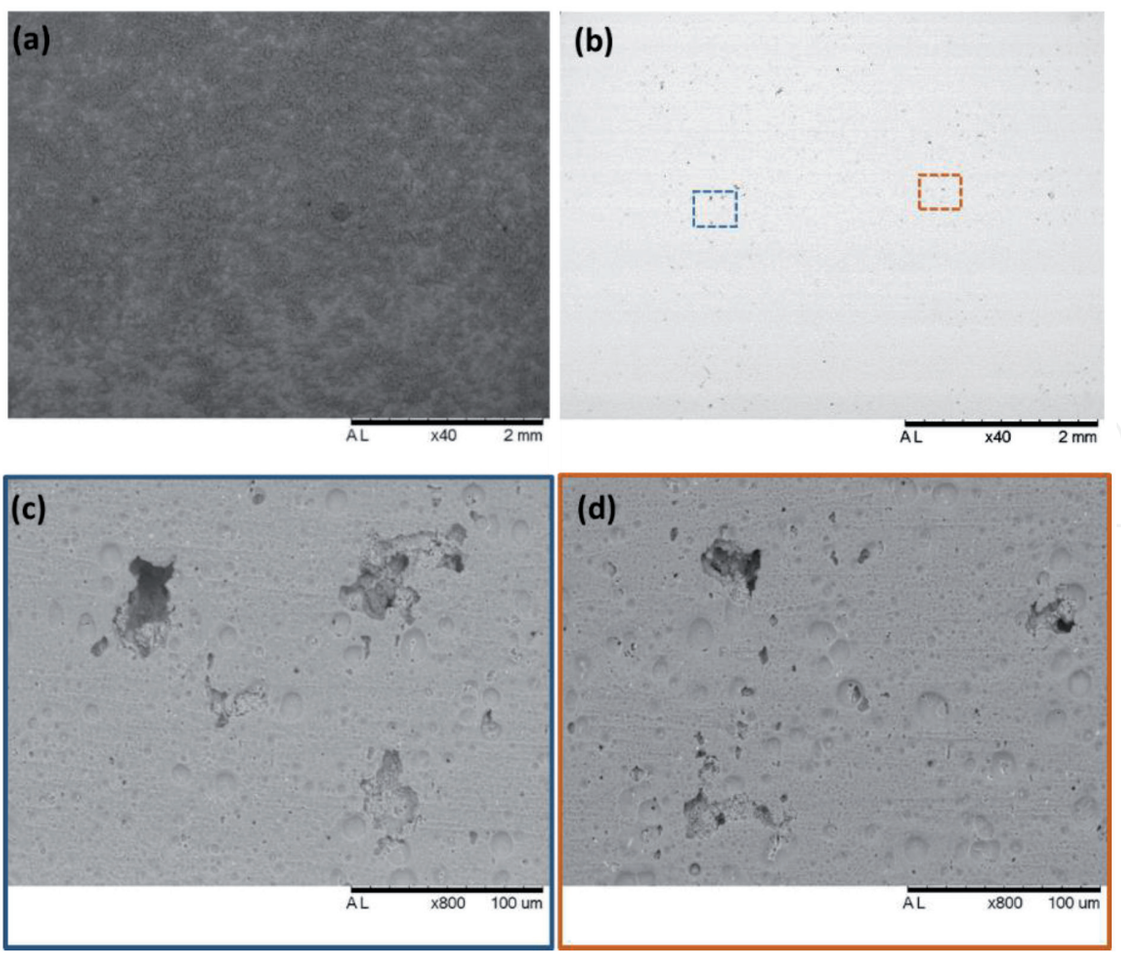

Figure 10.
SEM images of the corroded surface of AA2024-T3 alloy (a) before and (b–d) after the removal of corrosion products.

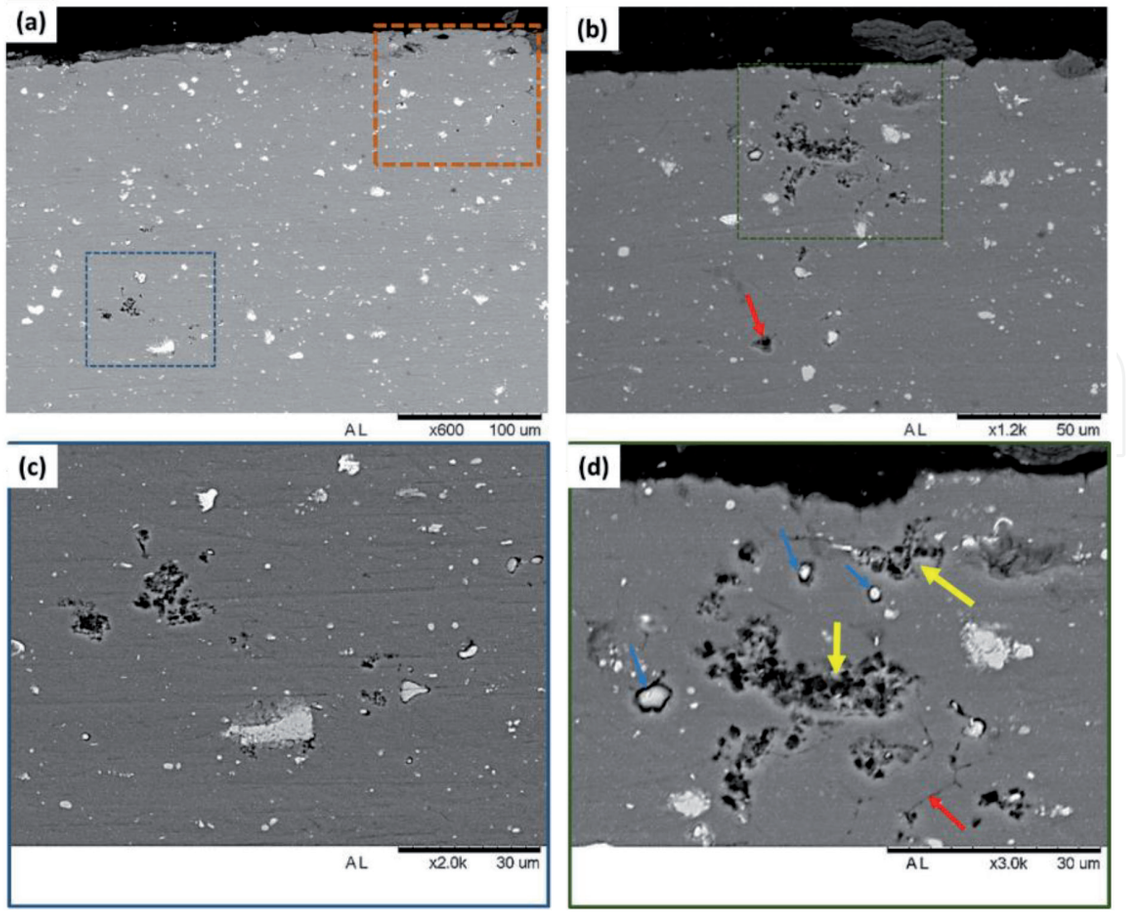

Figure 11.
SEM images of the cross-section of corroded AA2024-T3 alloy showing different depths and morphologies of attacks.

in a coarse particle has been previously reported in the literature [25, 29]. Micro-galvanic coupling can occur within HT particles [29], and the micro-galvanic interactions between the compositionally different domains in the particles (and the matrix) possibly resulted in the selective dissolution of the most active regions in the particles. These regions are most likely richer in Mg compared with the other regions, and are, therefore, anodic both to the matrix and the other regions of the particles. The HM particles were not found to be associated with any form of corrosion activities in this work. They are possibly (Al,Cu)x(Fe,Mn)ySi group of particles with lower Cu/Fe ratio as reported by Boag et al. [22] who also showed that trenches were not formed around these particles except after prolonged hours of exposure. The HC particles are Cu-enriched Al-Cu-Mg particles and Al-Cu-Fe-Mn particles. EDX analysis revealed that the Cu-enriched Al-Cu-Mg particles are dealloyed S-phase particles with Al and Mg contents in the range of 17 and 1.0 wt %, respectively, compared with 35.29 and 12.59 wt % of the HT particles. The selective leaching of the Al and Mg components resulted in the formation of Cu-rich remnants. The high Cu-content of the Al-Cu-Fe-Mn particles are associated with the re-deposition of Cu on these particles since they are cathodic particles [24]. The HC particles caused the dissolution of the adjacent matrix, and, hence, the formation of trenches.

From **Figure 11**, it is clear that there are links between the particle-associated attack and the GB attacks, and these links provide pathways for deep penetration into the alloy. However, it is important to note that the transition from pitting to intergranular corrosion is a typical corrosion characteristic of this alloy [30–32].

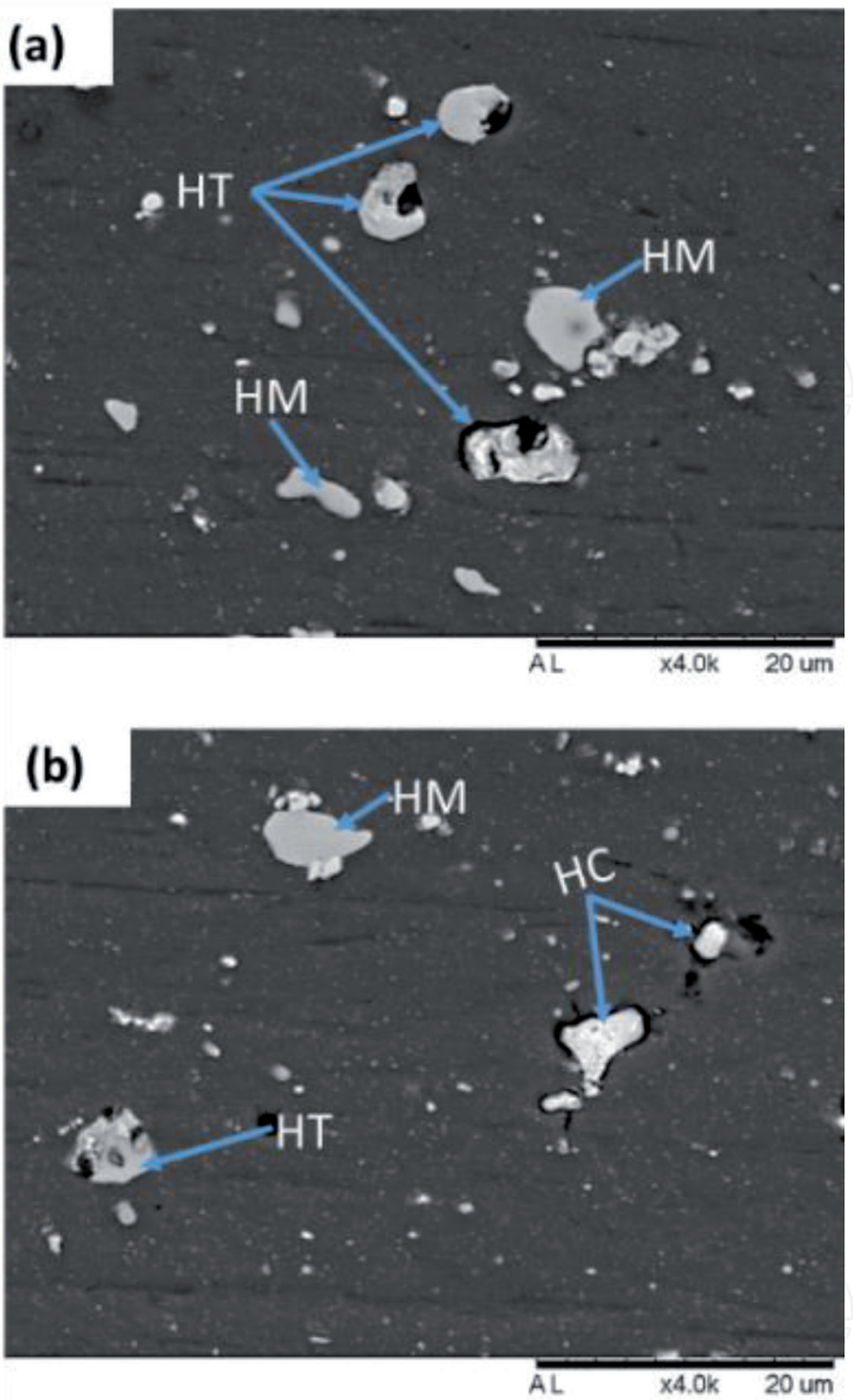

Figure 12.
SEM images of the cross-section of a corroded AA2024-T3 alloy showing different types of precipitates with respect to the corrosion activities. These images were obtained from areas within the brown square in ***Figure 11a****.*

Also, because of the non-linear form of these links, the attacks branch significantly such that it is often difficult to follow the attacks from the surface to regions far beneath the surface through cross-sectional examination.

Unlike the new generation alloys, especially the AA2098 and AA2198 alloys, the initiation of SLC in the AA2024-T3 alloy is associated with the coarse intermetallic phases, and the propagation of attack appears to have no relationship with the rolling direction. Also, far more SLC sites were observed on the AA2024-T3 alloy, and the attacks penetrated very deep into the alloy - twice as deep as those observed

on the new generation alloys (except for the AA2050-T84 alloy). This shows why the total current from the pits swamps that of the pseudopassive as observed on the polarization curves. Thus, it can be argued that the new generation Al-Cu-Li alloys (except for the AA2050-T84 alloy) are more corrosion resistant compared with the AA2024-T3 alloy.

3.2.3 AA6082-T6

Presented in **Figure 13** are SEM images showing the corroded surfaces of the AA6082-T6 alloy before and after the removal of corrosion products and the cross-sectional image obtained afterwards.

In this alloy, the predominant form of corrosion was trenching, and cavity (micro-pit) formation and this was associated with the activities of the coarse Fe-rich particles. The Fe-rich particles were the predominant coarse particles on this alloy. The formation of SLC was very rare. In fact, only a site was found in the entire area exposed, and it was not pronounced. The observed SLC was intergranular (**Figure 13d**) and penetrated only as deep as 30 μm. The formation of IGC in this alloy is as a result of the formation of Mg_2Si particles at the GBs with widened precipitate free zones (PFZs) [33] as typified in the TEM image in **Figure 14a**. The Mg_2Si (β) phase is highly anodic to the Al matrix [34, 35]. The absence of precipitates at regions immediately adjacent to the GBs promotes galvanic interactions between a highly anodic Mg_2Si phase and the PFZs. Upon exposure, the Mg component of the Mg_2Si phase is selectively dissolved leaving behind a Si-enriched particle

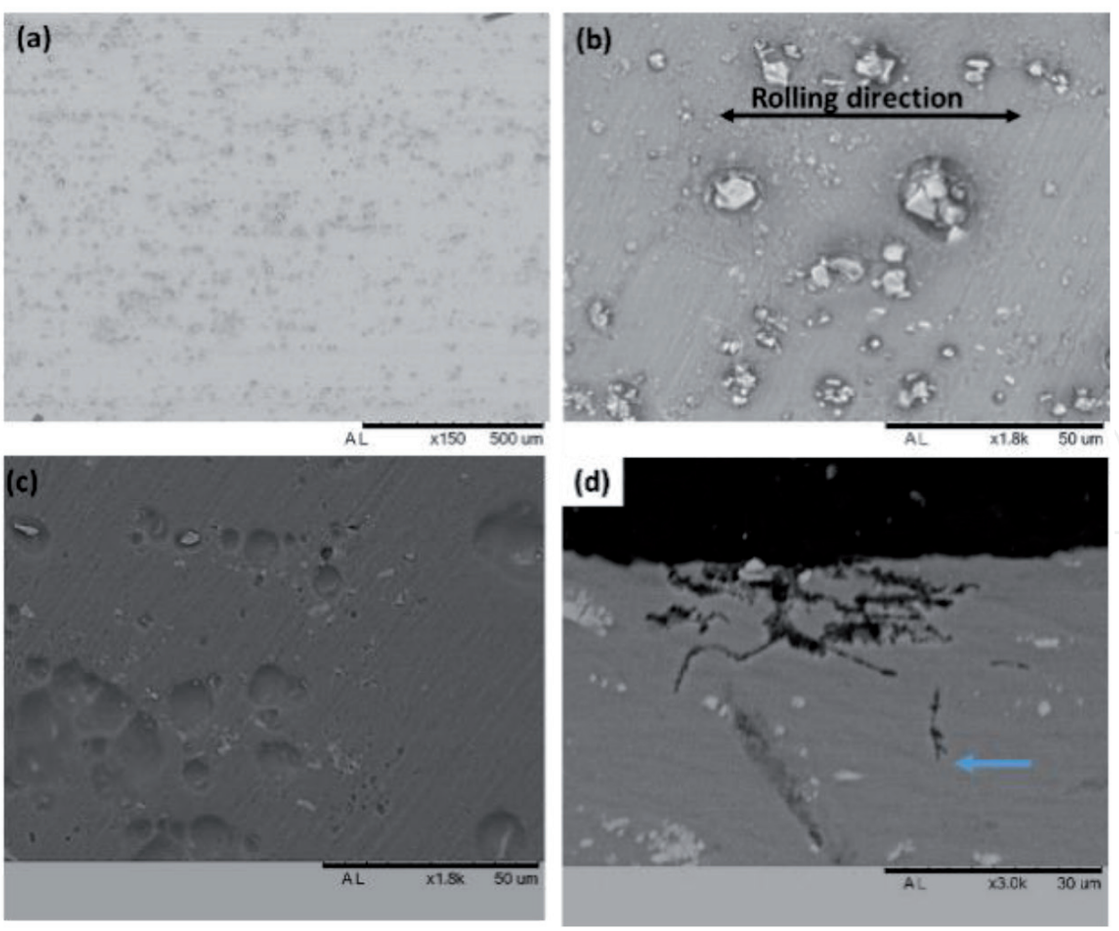

Figure 13.
SEM images of the corroded surface of AA6082-T6 alloy (a, b) before and (c) after the removal of corrosion products. (d) Cross-section of the corroded alloy showing the intergranular attack.

remnant. Although some authors have argued that Si-enriched particles rapidly form SiO_2 in the presence of water and are therefore not effective cathodes [36–38], it is believed that this remnant is cathodic and causes the dissolution of the adjacent PFZs [33, 39]. An example of the activities of the Si-enriched Mg_2Si particles can be seen in **Figure 14b, c**. The images provided were obtained from a mildly corroded region of an AA6082-T6 sample that was exposed to 3.5% NaCl solution for 7 days. The corrosion products were not removed before obtaining the images. From these images, it can be seen that the Si-enriched particles cause the dissolution of the adjacent matrix leading to the selective dissolution of the GB.

Nonetheless, the AA6082-T6 alloy is the most resistant to corrosion amongst the selected alloys compared—the number of SLC sites per area and the depth of SLC penetration were the lowest. This agrees with the SVET result.

3.2.4 AA7050-T7451

Figures 15 and **16** present the SEM images of the corroded surfaces (before and after the removal of corrosion products) and the cross-section of the AA7050-T7451 after the 72-h immersion test. **Figure 15b** is a magnified image of the marked region in **Figure 15a**. As with the other alloys, corrosion rings were also formed around SLC sites. However, except for the highly pronounced region of attack, the corrosion products blended well with the surface and covered

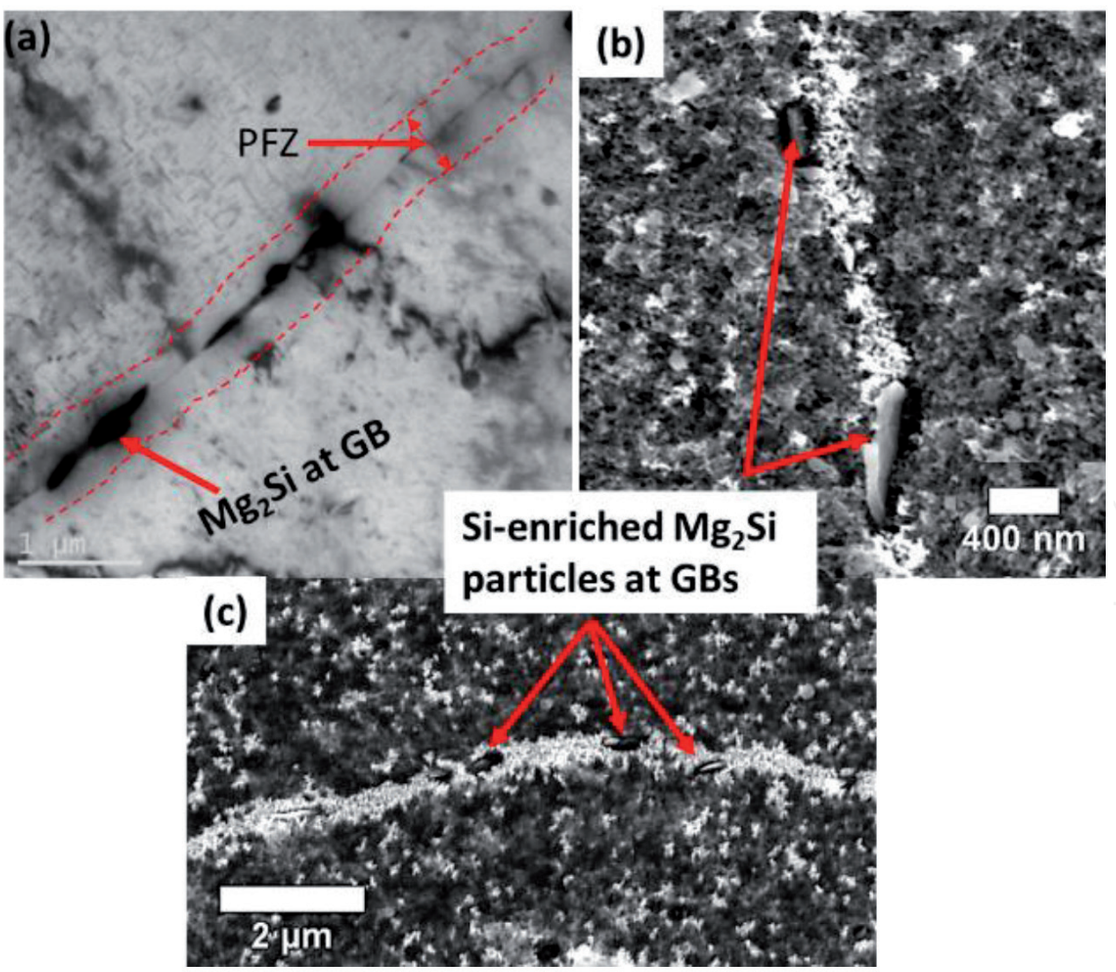

Figure 14.
(a) TEM bright-field image showing widened PFZ and Mg_2Si precipitates at the grain boundary of the AA6082-T6 alloy. (b) SEM images showing Si-enriched remnants at the GB of the corroded surface of AA6082-T6 alloy.

pitting sites smoothly. And this is the reason behind the glossy appearance of the surface at macro-scale (**Figure 6h**). After the removal of the corrosion products, pronounced SLC sites numbering up to 24 per cm^2 were revealed. The SLC was predominantly IGC, but other forms of intragranular corrosion were also observed (see **Figure 16c** and the region labeled z in **Figure 16d**). Furthermore, superficial IGC were observed across the entire surface examined (**Figure 16e**). It is clear from the images in Figure that the selective dissolution of the particles precipitated at the GBs plays an important role in the IGC attack. In the 7xxx series alloys, the η(Zn_2Mg) phase and its variants are usually associated with IGC [40–42]. This phase is highly active compared with the matrix of the alloys and preferentially dissolves upon exposure to aggressive media. The potential difference between a widened PFZ and the grain interior also plays a role in the selective dissolution of the GBs in 7xxx series alloys [43].

The SLC attacks propagated according to the elongation induced by the prior deformation process. The SLC attacks penetrated as deep as 143 μm into the alloy (**Figure 16f**). The SEM image in **Figure 16c** shows that the propagation of the SLC was also affected by grain specific bands similar to the grain features revealed by Donatus et al. [44, 45]. Again, superficial dissolution of regions around some pit mouths, similar to what was revealed on the AA2050 alloy, were observed. This further shows the effect of the local chemistry changes around the mouths of the pits.

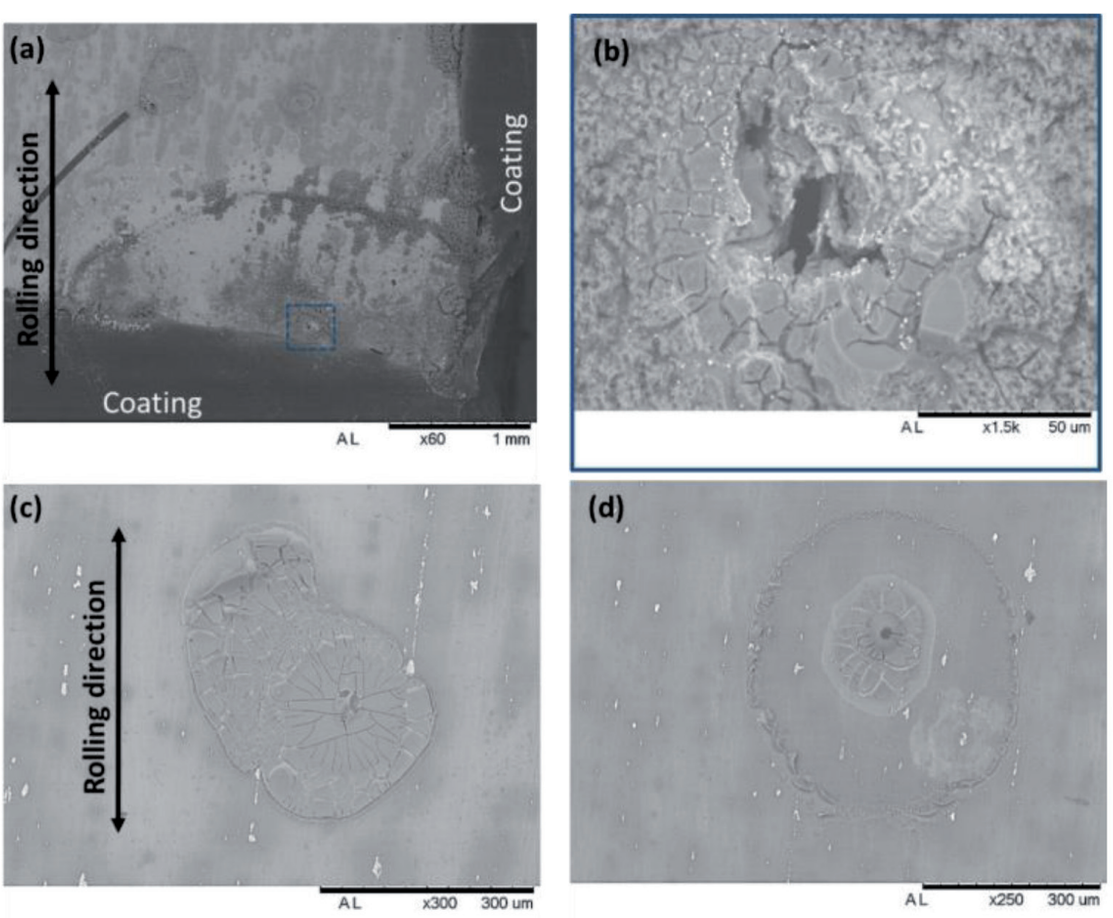

Figure 15.
SEM images of the corroded surface of AA7050-T7451 alloy before the removal of corrosion products showing different types of SLC sites on the alloy.

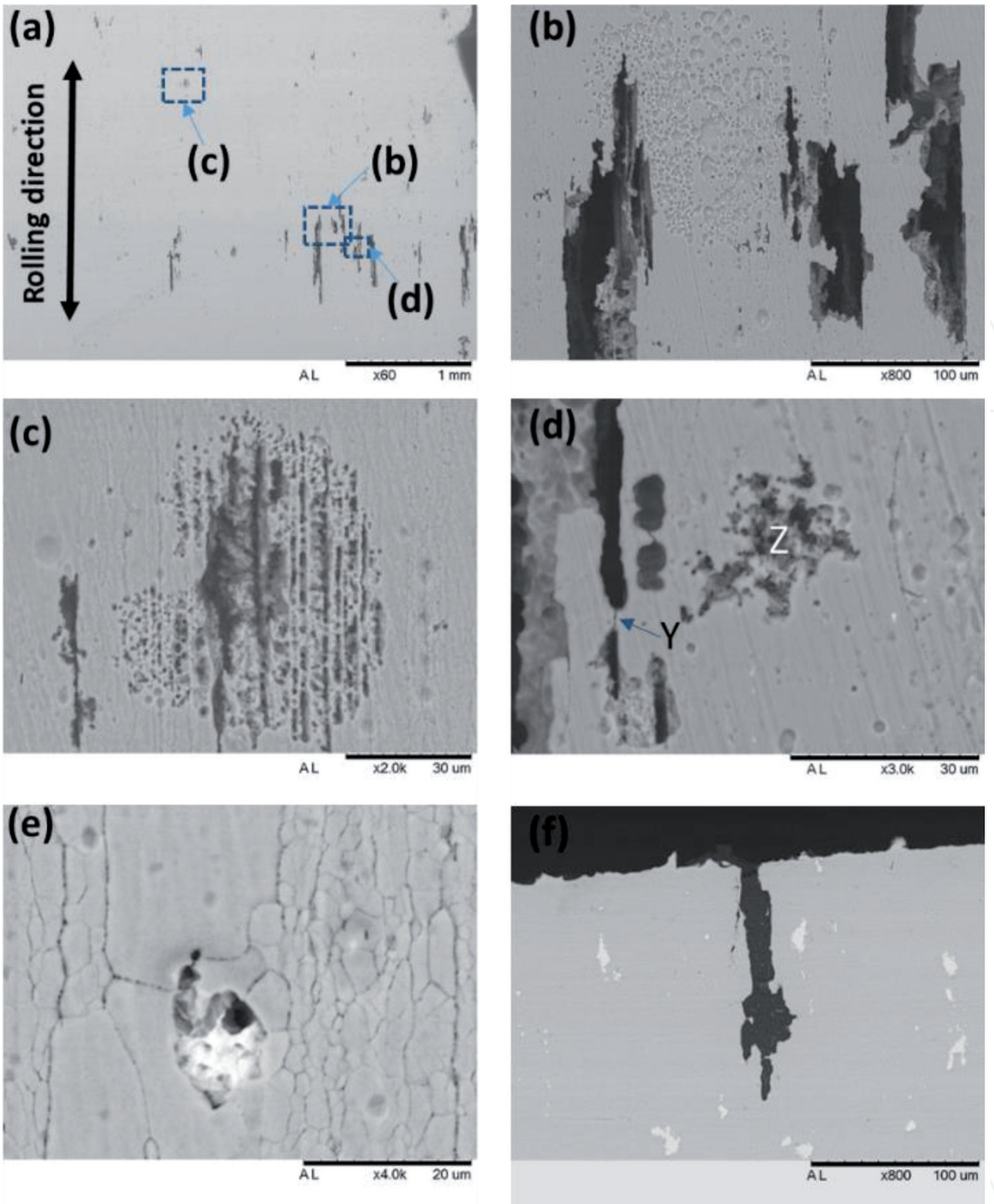

Figure 16.
SEM images of the corroded (a–e) surface and (f) cross-section of AA7050 alloy after the removal of corrosion products. Different forms of corrosion including a superficial form of intergranular attack (e) were observed.

Compared with the new-generation Al-Cu-Li alloys, the AA7050-T7451 alloy is far more susceptible to corrosion both in terms of depth of penetration (except for the AA2050-T84 alloy) and the number of attacks per cm^2. Also, the attack on AA7050-T7451 is far more insidious compared with all the alloys tested since it is very difficult to detect at macro-scale.

4. Summary

Table 2 gives a summary of the corrosion type, morphology and the microstructural features associated with the corrosion of the selected aluminum alloys.

Presented in **Figure 17a** are curves showing the peak depth of corrosion attack and the number of SLC sites per cm^2 for the selected alloys. In terms of depth of penetration, the most corrosion-resistant alloy is the AA6082-T6 alloy followed by the new-generation AA2098-T351, AA2198-T8 and AA2198-T851 alloys. The "51" treatment increased the susceptibility of the later alloys. The corrosion rate of the AA2050-T84 is the highest with the attack penetrating twice as deep as that of the nearest alloy (the AA2024-T3) alloy. In terms of the number of pits per cm^2, the AA2024-T3 presented the highest number followed by the AA7050-T7451 alloys. These two alloys, alongside the AA2050-T84 alloy, are the least corrosion-resistant alloys.

Figure 17b shows the length of the spread of SLC on the surfaces of the alloys. Although the new generation Al alloys are more resistant in terms of corrosion penetration and the number of pits per cm^2, these alloys presented the largest lengths of SLC attacks on the average. This was most evident in the AA2098-T351 alloy. These alloys only exhibited an intragranular form of attack and this form of attack only propagated and spread laterally, but predominantly according to the direction of deformation.

It is also important to note that the corrosion behaviors of the Al-Cu-Li alloys are not the same. Different factors trigger and promote SLC in these alloys. The AA2050-T84 alloy presented a very different degree of susceptibility and morphology in comparison with the other third-generation Al-Cu-Li alloys namely, the AA2098-T351, AA2198-T8 and the AA2198-T851 alloys. However, it is important to state that the AA2098 alloy is a precursor to the AA2198 alloy [46]. This probably explains why their corrosion behaviors are similar. It is also very evident from the results that, except for the AA6082-T6 alloy, every other alloy that exhibited IGC presented very high rates of corrosion attack penetration. The new generation Al-Cu-Li alloys (except for AA2050-T84) that exhibited only intragranular corrosion were more resistant to corrosion penetration.

Alloy	SLC type and morphology	Associated microstructural features/ phases
AA2050-T84	Predominantly IGC and pitting developed from IGC Deeply penetrating and less branched attack	GB enrichment [12, 13]. Redeposited Cu. Non-uniform precipitation of particles.
AA2098-T351	Intragranular attack (no IGC) Exfoliating layers in attacked grains. Shallow and laterally spreading attack.	Intragranular T1 particles.
AA2198-T8	Same as AA2098-T351.	Same as AA2098-T351.
AA2198-T851	Same as AA2098-T351 + band-like attack.	Same as AA2098-T351.
AA2024-T3	Predominantly IGC and pitting with particle consumption, and particle-GB linked attack. Deeply penetrating and highly branched attack.	S-phase and heterogeneous Cu-rich particles.
AA6082-T6	IGC Less pronounced penetration.	Mg_2Si (β) particles and precipitate free zones at GBs.
AA7050-T7451	IGC, pitting and intragranular band-like attack Deeply penetrating and less branched attack.	Zn_2Mg (η) and η-phase variants at GBs [40–42], and the presence of PFZs [43].

Table 2.
Summary of SLC type and morphology and associated microstructural features and phases in the alloys investigated.

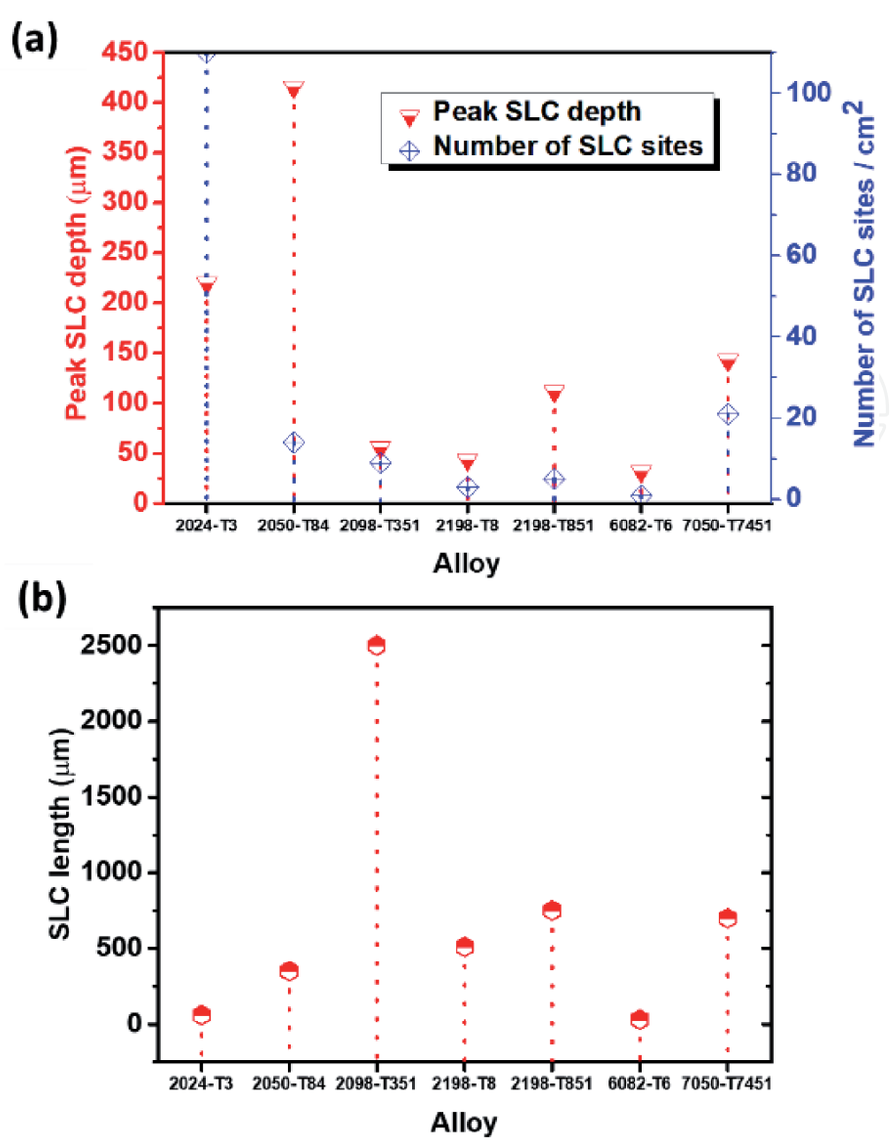

Figure 17.
Plots showing the observed (a) peak SLC depths and number of SLC sites per cm² and (b) peak lengths of SLC on the selected aluminum alloys.

Furthermore, there seems to be a strong relationship between the direction of attack propagation and spread with the direction of deformation. This was evident in at least five out of the seven alloys investigated. Also, all the alloys exhibited trenching and the formation of cavities (micro-pits). These types of attack are associated with the activities of cathodic coarse intermetallic particles.

In conclusion, the new generation aerospace alloys (except for the AA2050-T84) are more resistant to corrosion than the conventional aerospace alloys (AA2034-T3 and AA7050-T7451) but are less resistant compared with the AA6082-T6 alloy. It was difficult to fully establish these differences from electrochemical approaches (especially from the potentiodynamic polarization technique). Thus, it is advisable always to employ a non-electrochemical approach when the corrosion resistance of Al alloys are to be compared, and this can be combined with electrochemical techniques to gain more insight.

Acknowledgements

The authors appreciate FAPESP for financial support through the grant Proc. 2013/13235-6 and for sponsoring the postdoctoral fellowships of Dr. Uyime

Donatus (Process 2017/03095-3). The authors also wish to acknowledge the African Academy of Sciences Grant No [ARPDF 18-03], for providing financial support to carry out part of this research.

Author details

Uyime Donatus[1*], Michael Oluwatosin Bodunrin[2], Ayotunde Olayinka[3], Mariana Xavier Milagre[1], Olamilekan Rasaq Oloyede[4], Sunday Aribo[5], João Victor de Sousa Araujo[1], Caruline de Souza Carvalho Machado[1] and Isolda Costa[1]

1 Nuclear and Energy Research Institute, Sao Paulo, Brazil

2 School of Chemical and Metallurgical Engineering, University of the Witwatersrand, Johannesburg, South Africa

3 Louisiana Advanced Metal Processing Laboratory, Mechanical Engineering, University of Louisiana at Lafayette, Lafayette, Louisiana, USA

4 Institute for Materials Research, School of Chemical and Process Engineering, University of Leeds, UK

5 Research and Product Development, Evraz North America, Regina, SK, Canada

*Address all correspondence to: uyimedonatus@yahoo.com

References

[1] Moreto JA, Marino CEB, Bose Filho WW, Rocha LA, Fernandes JCS. SVET, SKP and EIS study of the corrosion behaviour of high strength Al and Al–Li alloys used in aircraft fabrication. Corrosion Science. 2014;**84**:30-41

[2] Moreto JA, Gamboni OC, Marino B, Bose Filho W, Fernandes S, Rocha LA. Corrosion behaviour of Al and Al-Li alloys used as aircraft materials. Corrosion and Protection of Materials. 2012;**31**(3/4):60-64. Available from: http://www.scielo.mec.pt/pdf/cpm/v31n3-4/v31n3-4a01.pdf [cited 20 July 2017]

[3] Garrard WN. Corrosion behavior of aluminum-lithium alloys. Corrosion. 1994;**50**(3):215-225. DOI: 10.5006/1.3293513

[4] Frankel G. The effects of microstructure and composition on Al alloy corrosion. Corrosion. 2015;**71**(11):1308-1320

[5] Donatus U, Terada M, Ospina CR, Queiroz FM, Fatima Santos Bugarin A, Costa I. On the AA2198-T851 alloy microstructure and its correlation with localized corrosion behaviour. Corrosion Science. 2018;**131**:300-309. DOI: 10.1016/j.corsci.2017.12.001

[6] de Sousa Araujo JV, Donatus U, Queiroz FM, Terada M, Milagre MX, de Alencar MC, et al. On the severe localized corrosion susceptibility of the AA2198-T851 alloy. Corrosion Science. 2018;**133**:132-140. DOI: 10.1016/j.corsci.2018.01.028

[7] Viramontes-Gamboa G, Rivera-Vasquez BF, Dixon DG. The active-passive behavior of chalcopyrite. Journal of the Electrochemical Society. 2007;**154**(6):C299-C311. DOI: 10.1149/1.2721782

[8] Burstein GT, Salter VCC, Ball J, Sharman JD. In: Datta M, MacDougall BR, Fenton JM, editors. The Growth of Pits during the Electrograining of Aluminium. Chicago, Illinois, USA: Electrochemical Society; 1996. Available from: https://books.google.com.br/books?id=P4TppG5uByoC&pg=PA133&lpg=PA133&dq=pseudopassive+behaviour+in+Al+alloys&source=bl&ots=FtQLepZJ2W&sig=ffZrJJn4a-KCydHErhyqy5cXy2o&hl=en&sa=X&ved=2ahUKEwjp1fmAhsDfAhVMCpAKHdKmCxsQ6AEwDXoECAkQAQ#v=onepage&q=pseudopassive [cited 26 December 2018]

[9] Tsuyuki C, Yamanaka A, Ogimoto Y. Phase-field modeling for pH-dependent general and pitting corrosion of iron. Scientific Reports. 2018;**8**(1):12777. Available from: http://www.nature.com/articles/s41598-018-31145-7

[10] Proton V, Alexis J, Andrieu E, Delfosse J, Deschamps A, De Geuser F, et al. The influence of artificial ageing on the corrosion behaviour of a 2050 aluminium-copper-lithium alloy. Corrosion Science. 2014;**80**:494-502

[11] Proton V, Alexis J, Andrieu E, Blanc C, Delfosse J, Lacroix L, et al. Influence of post-welding heat treatment on the corrosion behavior of a 2050-T3 aluminum-copper-lithium alloy friction stir welding joint. Journal of the Electrochemical Society. 2011;**158**(5):C139-C147

[12] Yan Y, Peguet L, Gharbi O, Deschamps A, Hutchinson CR, Kairy SK, et al. On the corrosion, electrochemistry and microstructure of Al-Cu-Li alloy AA2050 as a function of ageing. Materialia. 2018;**1**:25-36. Available from: http://linkinghub.elsevier.com/retrieve/pii/S2589152918300115

[13] Guérin M, Alexis J, Andrieu E, Laffont L, Lefebvre W, Odemer G, et al. Identification of the metallurgical parameters explaining the corrosion susceptibility in a 2050 aluminium alloy. Corrosion Science. 2016;**102**:291-300

[14] Buchheit RG, Moran JP, Stoner GE. Electrochemical behavior of the T1 (Al2CuLi) intermetallic compound and its role in localized corrosion of Al-2%Li-3%Cu alloys. Corrosion. 1994;**50**(2):120-130. DOI: 10.5006/1.3293500

[15] Luo C, Albu SP, Zhou X, Sun Z, Zhang X, Tang Z, et al. Continuous and discontinuous localized corrosion of a 2xxx aluminium-copper-lithium alloy in sodium chloride solution. Journal of Alloys and Compounds. 2016;**658**:61-70. DOI: 10.1016/j.jallcom.2015.10.185

[16] Ma ZY, Zhou X, Liao Y, Yi Y, Wu H, Wang Z, et al. Localised corrosion in AA 2099-T83 aluminium-lithium alloy: The role of grain orientation. Corrosion Science. 2015;**107**:41-48

[17] Donatus U, Klumpp RE, Mogili NVV, Aletobelli Antunes R, Milagre MX, Costa I. The effect of surface pretreatment on the corrosion behaviour of silanated AA2198-T851 Al-Cu-Li alloy. Surface and Interface Analysis. 2019;**51**(2):275-289

[18] Zhang X, Zhou X, Hashimoto T, Liu B, Luo C, Sun Z, et al. Corrosion behaviour of 2A97-T6 Al-Cu-Li alloy: The influence of non-uniform precipitation. Corrosion Science. 2018;**132**:1-8. Available from: https://www.sciencedirect.com/science/article/pii/S0010938X1730896X [cited 20 January 2018]

[19] Donatus U, Ferreira RO, Vardan Mogili NV, Gonçalves de Viveiros BV, Milagre MX, Costa I. Corrosion and anodizing behaviour of friction stir weldment of AA2198-T851 Al-Cu-Li alloy. Materials Chemistry and Physics. 2018;**219**(August):493-511. Available from: https://linkinghub.elsevier.com/retrieve/pii/S0254058418307193

[20] Donatus U, de Sousa Araujo JV, de Souza Carvalho Machado C, Vardhan Mogili NV, Antunes RA, Costa I. The effect of manufacturing process induced near-surface deformed layer on the corrosion behaviour of AA2198-T851 Al–Cu–Li alloy. Corrosion Engineering, Science and Technology. 2018;**2782**:1-11. DOI: 10.1080/1478422X.2018.1558932

[21] Donatus U, de Viveiros BVG, de Alencar MC, Ferreira RO, Milagre MX, Costa I, et al. Correlation between corrosion resistance, anodic hydrogen evolution and microhardness in friction stir weldment of AA2198 alloy. Materials Characterization. 2018;**144**:99-112. Available from: https://linkinghub.elsevier.com/retrieve/pii/S1044580318317546

[22] Boag A, Hughes A, Glenn A. Corrosion of AA2024-T3 part I: Localised corrosion of isolated IM particles. Corrosion. 2011;**53**(1):17-26. DOI: 10.1016/j.corsci.2010.09.009

[23] Glenn A, Muster T, Luo C, Zhou X, Thompson GE, Boag A, et al. Corrosion of AA2024-T3. Part III: Propagation. Corrosion Science. 2011;**53**(1):40-50. DOI: 10.1016/j.corsci.2010.09.035

[24] Chen GS, Gao M, Wei RP. Microconstituent-induced pitting corrosion in aluminum alloy 2024-T3. Corrosion. 1996;**52**(1):8-15

[25] Schneider O, Ilevbare GO, Scully JR, Kelly RG, Schneider O, Kelly RG, et al. In situ confocal laser scanning microscopy of AA 2024-T3 corrosion metrology. Journal of the Electrochemical Society. 2004;**151**(8):B465. DOI: 10.1149/1.1764781

[26] Zhou X, Luo C, Hashimoto T, Hughes AE, Thompson GE. Study of localized corrosion in AA2024 aluminium alloy using electron tomography. Corrosion Science. 2012;**58**:299-306. Available from: http://www.sciencedirect.com/science/article/pii/S0010938X12000807 [cited 18 March 2015]

[27] Hughes AE, Parvizi R, Forsyth M. Microstructure and corrosion of AA2024. Corrosion Reviews. 2015;**33**(1-2):1-30

[28] Dimitrov N, Mann JA, Vukmirovic M, Sieradzki K. Dealloying of Al_2CuMg in alkaline media. Journal of the Electrochemical Society. 2000;**147**(9):3283. DOI: 10.1149/1.1393896

[29] Queiroz F, Magnani M, Costa I, De MH. Investigation of the corrosion behaviour of AA 2024-T3 in low concentrated chloride media. Corrosion Science. 2008;**50**:2646-2657. Available from: http://www.sciencedirect.com/science/article/pii/S0010938X08002278 [cited 26 May 2013]

[30] Zhang W, Frankel G. Localized corrosion growth kinetics in AA2024 alloys. Journal of the Electrochemical Society. 2002;**149**(11):1-11. Available from: http://jes.ecsdl.org/content/149/11/B510.short [cited 09 May 2013]

[31] Zhang W, Frankel G. Anisotropy of localized corrosion in AA2024-T3. Electrochemical and Solid-State Letters. 2000;**3**(6):268. Available from: http://esl.ecsdl.org/content/3/6/268.short [cited 08 November 2012]

[32] Zhang W, Frankel G. Transitions between pitting and intergranular corrosion in AA2024. Electrochimica Acta. 2003;**48**(9):1193-1210. Available from: http://linkinghub.elsevier.com/retrieve/pii/S0013468602008289 [cited 28 October 2012]

[33] Donatus U, Thompson GE, Zhou X, Wang J, Cassell A, Beamish K. Corrosion susceptibility of dissimilar friction stir welds of AA5083 and AA6082 alloys. Materials Characterization. 2015;**107**:85-97. Available from: http://linkinghub.elsevier.com/retrieve/pii/S1044580315002491 [cited 10 July 2015]

[34] BirbilisN,BuchheitRG.Electrochemical characteristics of intermetallic phases in aluminum alloys an experimental survey and discussion. Journal of the Electrochemical Society. 2005;**152**(4):B140-B151. Available from: http://jes.ecsdl.org/content/152/4/B140%5Cn; http://jes.ecsdl.org/content/152/4/B140.full.pdf%5Cn; http://jes.ecsdl.org/content/152/4/B140.short

[35] Gupta RK, Sukiman NL, Fleming KM, Gibson MA, Birbilis N. Electrochemical behavior and localized corrosion associated with Mg_2Si particles in Al and Mg alloys. ECS Electrochemistry Letters. 2012;**1**(1): C1-C3. DOI: 10.1149/2.002201eel

[36] Svenningsen G, Larsen MH, Walmsley JC, Nordlien JH, Nisancioglu K. Effect of artificial aging on intergranular corrosion of extruded AlMgSi alloy with small Cu content. Corrosion Science. 2006;**48**(6):1528-1543

[37] Svenningsen G, Larsen MH, Nordlien JH, Nisancioglu K. Effect of thermomechanical history on intergranular corrosion of extruded AlMgSi(Cu) model alloy. Corrosion Science. 2006;**48**(12):3969-3987. Available from: http://linkinghub.elsevier.com/retrieve/pii/S0010938X06000989 [cited 04 March 2015]

[38] Liang WJ, Rometsch PA, Cao LF, Birbilis N. General aspects related to the corrosion of 6xxx series aluminium alloys: Exploring the influence of Mg/

Si ratio and Cu. Corrosion Science. 2013;**76**:119-128. DOI: 10.1016/j.corsci.2013.06.035

[39] Eckermann F, Suter T, Uggowitzer PJ, Afseth A, Schmutz P. The influence of MgSi particle reactivity and dissolution processes on corrosion in Al-Mg-Si alloys. Electrochimica Acta. 2008;**54**(2):844-855

[40] Wadeson DA, Zhou X, Thompson GE, Skeldon P, Oosterkamp LD, Scamans G. Corrosion behaviour of friction stir welded AA7108 T79 aluminium alloy. Corrosion Science. 2006;**48**(4):887-897. Available from: http://www.scopus.com/inward/record.url?eid=2-s2.0-33645025920&partnerID=tZOtx3y1 [cited 13 November 2014]

[41] Huang TS, Frankel GS. Kinetics of sharp intergranular corrosion fissures in AA7178. Corrosion Science. 2007;**49**(2):858-876

[42] Lu X, Han X, Du Z, Wang G, Lu L, Lei J, et al. Effect of microstructure on exfoliation corrosion resistance in an Al-Zn-Mg alloy. Materials Characterization. 2018;**135**:167-174. DOI: 10.1016/j.matchar.2017.11.029

[43] Marlaud T, Malki B, Henon C, Deschamps A, Baroux B. Relationship between alloy composition, microstructure and exfoliation corrosion in Al-Zn-Mg-Cu alloys. Corrosion Science. 2011;**53**(10):3139-3149. DOI: 10.1016/j.corsci.2011.05.057

[44] Donatus U, Thompson GE, Zhou X, Alias J, Tsai I-LL. Grain distinct stratified nanolayers in aluminium alloys. Materials Chemistry and Physics. 2017;**188**:109-114. DOI: 10.1016/j.matchemphys.2016.12.021

[45] Donatus U, Thompson GE, Elabar D, Hashimoto T, Morsch S. Features in aluminium alloy grains and their effects on anodizing and corrosion. Surface and Coatings Technology. 2015;**277**:91-98. Available from: http://linkinghub.elsevier.com/retrieve/pii/S025789721530147X [cited 25 July 2015]

[46] Fei ZS, Dong ZW, Hua YW, Ling SC, Jun WH. Ageing response of a Al-Cu-Li 2198 alloy. Materials and Design. 2014;**63**(April):368-374. DOI: 10.1016/j.matdes.2014.04.063